Chapter 3

DETECTOR

3.1 Detector Overview

This section provides an overview of a possible detector design to attain the physics goals of JLC-I.

Since the interaction region at JLC will be occupied by only one detector at one time, we consider a general purpose detector which allows precision tracking in a solenoidal magnetic field, hermetic calorimetry, and high resolution vertex detection. The detector is also required to be capable of operation under completely new background environments, and of the unambiguous identification of new physics that we shall encounter.

One of the most important characteristic features of e^+e^- experiment in this energy region is that all physics processes can be recognized in terms of known fundamental particles (leptons, quarks, and gauge bosons). To make maximum use of this advantage, we have to design our detector so as to exclusively reconstruct all final-state particles except neutrinos. Reconstruction of W and Z via jet invariant masses is very important in order to use their large decay branching fractions into quarks. To improve the mass resolution of the W and Z, we rely primarily on the tracking information for charged particles, though, of course, neutral particles are only detectable by the calorimeter. In this scheme, a good track-cluster matching is essential to determine the event topology correctly. It is also very important to tag b-quarks by vertex detection in order to study top and Higgs.

One of the most important physics targets of JLC is to find and study the intermediate mass Higgs. For this purpose, the detector should be capable of confirming the narrow decay width of the new particle. In searches for SUSY particles, detection of missing P_t is also important, and this requires a good angular coverage. Taking these requirements into account, we set the following design criteria:

1. hermetic calorimetry in the polar angle region $|\cos\theta| < 0.98$ (the rest is occupied by the final focus system),

2. jet invariant mass resolution comparable with the natural widths of the W and Z,

3. lepton pair recoil mass resolution for $e^+e^- \to ZH_{SM}$ comparable with the beam energy spread of $\sim$ 200MeV.

Fig. 3.1 shows the configuration of a detector that can be realized with modest extensions of the presently available technology. Table 3.1 summarizes the parameters and the performance

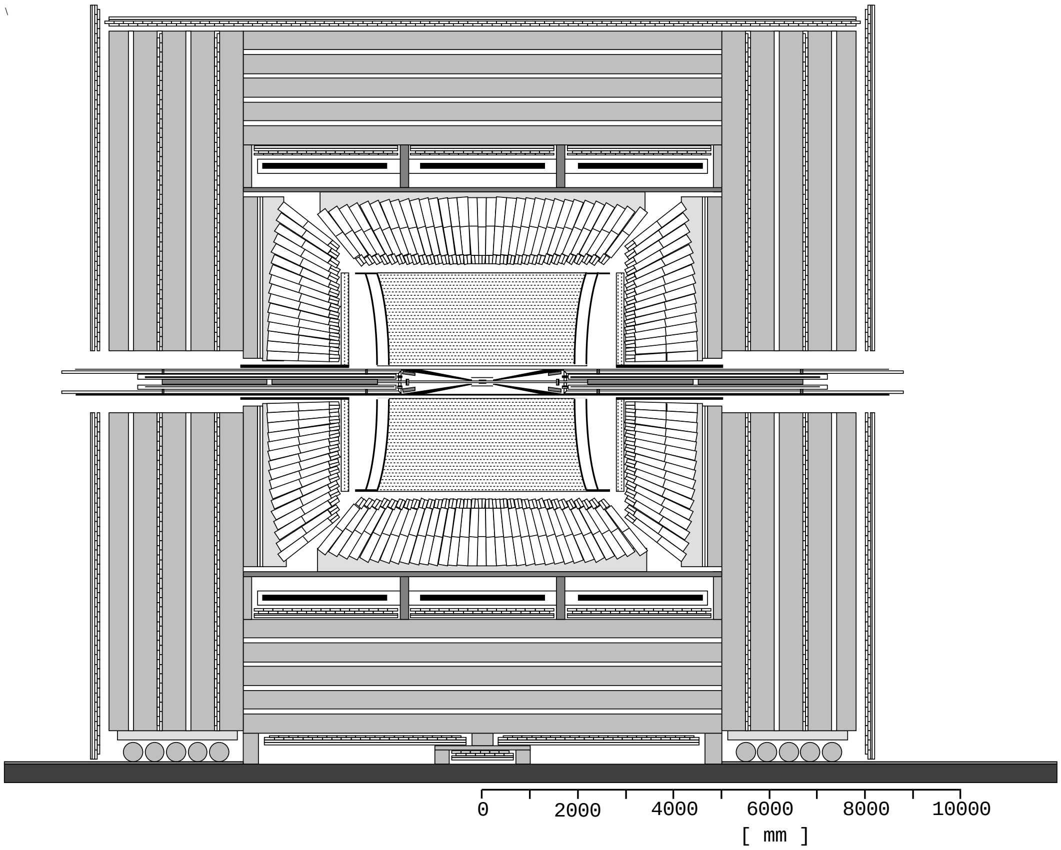

Figure 3.1: Schematical drawing of the JLC detector

DETECTOR	TYPE	CONFIGURATION	PERFORMANCE
VTX (Vertex Detector)	Silicon CCD	Pixel Size ; 25 μm Number of Layers ; 2 layers Layer Position ; r=2.5cm & 7.5cm Thickness ; 500 μm / layer $\mid \cos\theta \mid < 0.95$	Position Resolution ; $\sigma = 7.2\ \mu$m Impact Parameter Resolution δ [μm]; $\delta^2 = 11.4^2 + (28.8/p)^2 / \sin^3\theta$
CDC (Central Drift Chamber)	Small-cell Jet Chamber	Radius ; r = 0.3 - 2.3 m Length ; l = 4.6 m Number of Sampling = 100 $\mid \cos\theta \mid < 0.70$ (full sampling) $\mid \cos\theta \mid < 0.95$ (20 samplings)	Position Resolution ; $\sigma_x = 100\ \mu$m (/ axial wire) $\sigma_z = 2$ mm (/ stereo wire) Momentum Resolution ; $\sigma_{Pt} / Pt = 1.1 \times 10^{-4} Pt \oplus 0.1\%$ $\sigma_{Pt} / Pt = 5 \times 10^{-5} Pt \oplus 0.1\%$ (with vertex constraint)
CAL	Lead + Plastic Scintillator Sandwitch (Compensated)	EM part ; thickness = 29 Xo cell size = 10cm x 10cm HAD part ; thickness = 5.6 λo cell size = 20cm x 20cm Si Pad ; pad size = 1cm x 1cm $\mid \cos\theta \mid < 0.99$	Energy Resolution ; $\sigma_E / \sqrt{E} = 15\% / \sqrt{E} \oplus 1\%$ (e & γ) $\sigma_E / \sqrt{E} = 40\% / \sqrt{E} \oplus 2\%$ (hadron) Si Pad Position Resolution ; $\sigma = 3$ mm Si Pad e/π Rejection = 1/50
MUON	Single Cell Drift Chamber	Number of Superlayers ; 6 $\mid \cos\theta \mid < 0.99$	Position Resolution ; $\sigma = 500\ \mu$m Pt > 3.5 GeV (barrel)

* All momentum and energy are expressed in [GeV].

Table 3.1: Parameters and performances of the JLC detector

of each detector component. All the tracking devices and the calorimeter are placed inside the 2-Tesla superconducting solenoid to achieve a good hermeticity.

Vertex detector (VTX) : The vertex detector consists of 2 layers of Si-CCD arrays that can accomodate background tracks and γ's due to e^+e^- pairs created by beamstrahlung photons. The first and the second layers are placed at r=2.5cm and r=7.5cm, respectively, and the expected impact parameter resolution is 30 μm (90°, p=1GeV/c).

Central drift chamber (CDC) : The central tracking detector is a small-cell jet chamber. The inner and outer radii are 30cm and 230cm, respectively, and 100 points are sampled with a spatial resolution of 100μm. To use maximally the charged track information, we require two-track separation capability of 1mm. The resolution in the z-coordinate is designed to be less than 2mm at the front face of the calorimeter to achieve a good track-cluster matching.

Calorimeter (CAL) : The calorimeter is of a lead-scintillator sandwich type that has an equal response to electromagnetic and hadron showers. The calorimeter is longitudinally segmented into three sections: the fine sampling electromagnetic shower section of 29 X_0 thickness (ECAL), Si-pads to detect electromagnetic pre-showers located after the first 4.3 X_0 of ECAL, and a hadron section of 5.6 interaction lengths (HCAL). The barrel and the endcap calorimeters consist of 2500 and 1250 tower modules, each pointing to the interaction region.

Muon detector (Muon) : The muon detector consists of six super-layers of single cell drift chambers. Since it only provides muon identification, a modest spatial resolution of 500 μm is required. The threshold momentum for muon identification is 3.5 GeV/c due to the large energy loss in the calorimeter.

The interaction region is quite different from those we have experienced at the storage ring experiments. To get a stable collision of nanometer-size beams, we have to control the final quadrupole magnets with comparable accuracy. In this detector design, the Q-magnets of both electron and positron sides are fixed in the same cylinder made of CFRP to cancel common mode vibrations. Inside the cylinder, the magnet positions are monitored by laser interferometers whose signals are fed back to piezo transducers for precision active alignment.

Background arising from beam-beam interactions has been systematically studied for both QED and QCD processes. The beam mask configuration shown in Fig. 3.2 is designed to effectively shield the most troublesome soft photons from e^+e^- pairs created by beam-beam interactions.

3.2 Vertex Detector

3.2.1 Requirements for the Vertex Detector

The vertex detector (VTX) measures the track positions of charged particles very precisely near the interaction point. The major role of the VTX is to reconstruct the secondary and tertiary decay vertices from B and D meson decays, to tag b- or c-quark jets. The b-quark jet tagging is of essential importance, particularly in the search for the intermediate mass Higgs ($m_H \sim 100$ GeV), as discussed in section 2.2. The VTX should have a spatial (or impact parameter) resolution good enough to get a high rejection ratio for light quark jets, while keeping a good efficiency for b-quark jets.

The VTX also plays an important role in the momentum measurements of charged particles. Since the VTX has much better spatial resolution than the central drift chamber (CDC), it puts a strong constraint on the track fitting and improves the momentum resolution by a factor of two. The effect of the VTX constraint will be discussed in detail in section 3.3.

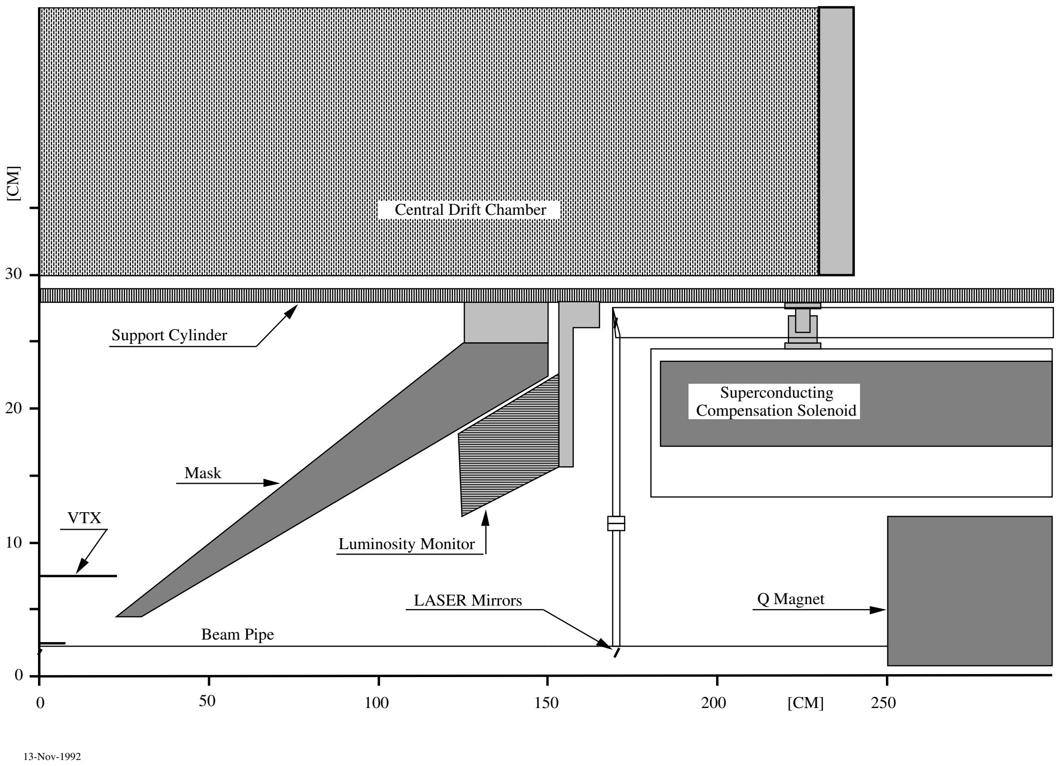

Figure 3.2: Layout of the interaction region

As the energy increases, particles in the jets become more and more collimated. Since the VTX is located close to the interaction point, the track density in the VTX is quite high. For unambiguous track reconstruction, the detector should be able to measure two-dimensional points rather than their projections. Therefore, pixel detectors should be used for the VTX.

3.2.2 Configuration

The VTX consists of two concentric layers of silicon pixel detectors made of charge coupled devices (CCDs). The impact parameter resolution can be written as

$$\delta^2 = \sigma^2\{(\frac{r_{out}}{r_{out}-r_{in}})^2 + (\frac{r_{in}}{r_{out}-r_{in}})^2\} + (\frac{0.014 r_{in}}{p\beta})^2 \frac{X_r}{\sin^3\theta},$$

where p is the momentum of the charged particle in GeV/c, r_{in} and r_{out} are the radii of the inner and outer layers, X_r is the thickness of the inner layer (including the beam pipe) in radiation lengths, and σ is the resolution of the vertex detector. The first term comes from measurement error and the second term from multiple scattering. This equation tells us that we should put the inner layer as close to interaction point as possible and outer layer as far as possible. However there are several constraints on the radii. First of all, the radius of the inner layer should be large enough to avoid the background from low-energy e^+e^- pairs created by beam-beam interactions (see section 3.7). As for the radius of the outher layer, we should take into account the cost of the VTX which increases $\propto r_{out}^2$, while the gain in resolution is little. In addition, the precise supporting and alignment of the VTX becomes more difficult for a larger size, and the resolution might get worse, if r_{out} is too large. Therefore the present design adopts

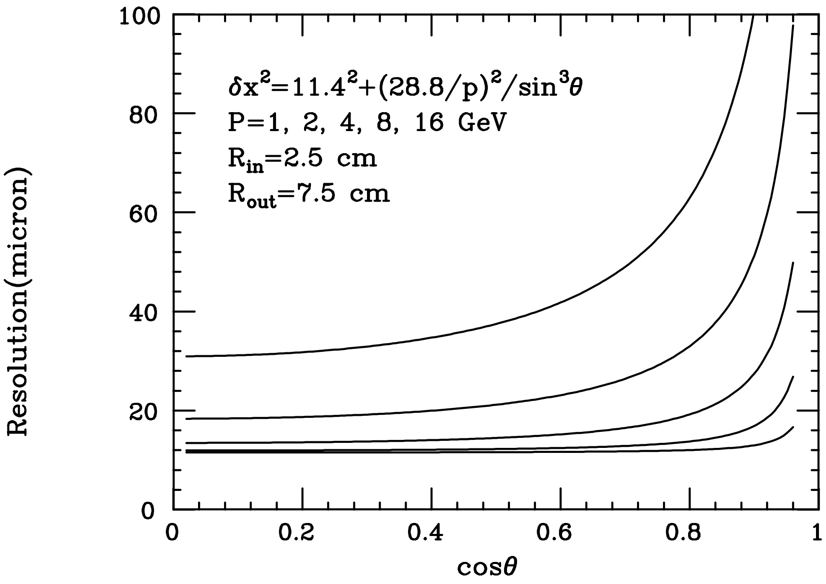

Figure 3.3: Impact parameter resolution as functions of momentum p and $\cos\theta$.

the following parameters. The inner and the outer layers are at $r_{in} = 2.5$ cm and $r_{out} = 7.5$ cm. It covers the angular region of $|\cos\theta| < 0.95$. The total lengths in the z-direction are ± 7.6 cm for the inner layer and ± 22.8 cm for the outer layer. The pixel size is 25 μm $\times$ 25 μm, which corresponds to a spatial resolution of 7.2 μm. If the center-of-gravity method works, we can get still better resolution. The total area of the CCDs is ~ 2400 cm^2, and the total number of pixels is $\sim 4 \times 10^8$. For these parameters, the impact parameter resolution becomes

$$\delta^2 = 11.4^2 + (28.8/p\beta)^2/\sin^3\theta \ (\mu\text{m}^2).$$

The impact parameter resolution δ is plotted as functions of $\cos\theta$ for several momenta in Fig. 3.3.

3.2.3 Operation of CCD Detectors

The CCDs will be operated close to room temperature (*i.e.* $> 0°$C). In general, operating CCDs at room temperature causes large dark currents (dark current increases exponentially as temperature goes up) and hence a large shot noise which is a serious problem in the detection of minimum ionizing particles (m.i.p.). Furthermore, the non-uniformity of dark currents causes a non-flatness of the output baseline. These problems, however, can be avoided by the following methods:

1. Since the shot noise is a statistical fluctuation of the integrated charge coming from dark currents ($\propto \sqrt{i_d t}$), this can be reduced by a quick readout.

2. If the signal charge is large enough, an increase in the noise does not matter so much. This can be achieved by making the depletion region thicker than the present CCDs used for video cameras.

At JLC-I, beam bunch trains make crossings at intervals of 6.7 ms (150 Hz). Each CCD is read out during this period almost continuously. By reading out continuously, each pixel in the same vertical line accumulates the same amount of charge due to dark currents, and the pattern of the baseline non-flatness is the same for every horizontal line. Therefore, the non-flatness can be corrected easily by subtracting the pattern of non-flatness which is stored in a analog shift register. If a dark current of 5 nA/cm^2 is assumed, the average shot noise becomes about 40 electrons. This number is comparable to other noise sources.

The thickness of the depletion region can be extended to $\sim 30\mu$m using high resistivity ($\sim$ 1 kΩcm) silicon wafers without a serious increase in dark currents due to defects in the crystal. In this case, more than 2000 electrons can be obtained for a m.i.p. track. If defect free silicon wafers with higher resistivity become available in the future, we can get CCDs with a still thicker depletion region.

The area of each CCD has to be small enough to be read out in 6.7 ms. If the same rate as for the present CCDs for video cameras is assumed, ~ 0.4 cm^2 can be read out in this period. Since the total area of the VTX is ~ 2400 cm^2, the number of readout channels is 6×10^3.

Collected charge from each pixel is shifted to the output node and read out through on-chip FETs. The output signal is processed through a correlated double sampling (CDS) circuit to eliminate reset noise, corrected for the non-flatness of the baseline, and digitized by a flash ADC. The ADC data and pixel address are stored in the memory, if the ADC counts exceed a certain threshold.

3.2.4 Expected Performance

There are two approaches of selecting b-quark jets using the VTX. One method is to select b jets exclusively by identifying the successive decay vertices of B and D mesons. The other way is to select heavy flavor jets by requiring that a certain number of tracks have a finite impact parameter (heavy flavor tagging). The latter method is, compared with the former one, easier and more efficient, though it is impossible to separate c- and b-quark jets clearly.

We have made a simulation of the heavy flavor tagging by impact parameter method, assuming the VTX described above. Two-jet events $e^+e^-(\sqrt{s} = 90 \text{ GeV}) \to u\bar{u},\ s\bar{s},\ c\bar{c},\ b\bar{b}$ are generated and charged particle tracks are smeared according to the resolution of the vertex detector. In order to tag the heavy flavor jet, we search for tracks which do not originate from the interaction point (I.P.). If a jet has more than two (or three) charged tracks with an impact parameter in the three-dimensional space b which satisfies $b/\sigma > \sigma_{cut}$, where σ is the impact parameter resolution expected from the momentum and angle, the jet is regarded as a heavy flavor jet. If the invariant mass of the two tracks is consistent with the mass of the K_S, those tracks are rejected. Fig. 3.4 shows distributions of the normalized impact parameter for the charged particles from the primary vertex (I.P.) and for the secondary and tertiary vertices (B or D decay). Tagging efficiency is plotted in Fig. 3.5 for s-, c-, and b-quark jets as functions of σ_{cut}. The tagging efficiency for b-quark jets is 78% (63%) if at least two (three) tracks are required to have impact parameters $b/\sigma > 2.5$. For a light quark jet, if we require at least two (three) tracks with $b/\sigma > 2.5$, the tagging efficiency is $\sim 0.5\%$ (0.25%), which means the light quark jets can be suppressed by a factor of 200 (400). It should be noted that the efficiency for the c-quark jet is much lower than the b-quark jet due to its shorter decay length and we can expect a suppression of the c-quark jets to some extent. If one tries to discriminate b-quark jets from c-quark jets more distinctively, more cuts, which could reduce the efficiency, are necessary. For a suppression of the W-pair background in $H \to b\bar{b}$, however, heavy flavor tagging works well enough because the decay mode $W \to c\bar{b}$, which can not be suppressed enough by the heavy flavor tagging, has a very small branching ratio ($|V_{cb}| \sim 0.05$). If we take the product

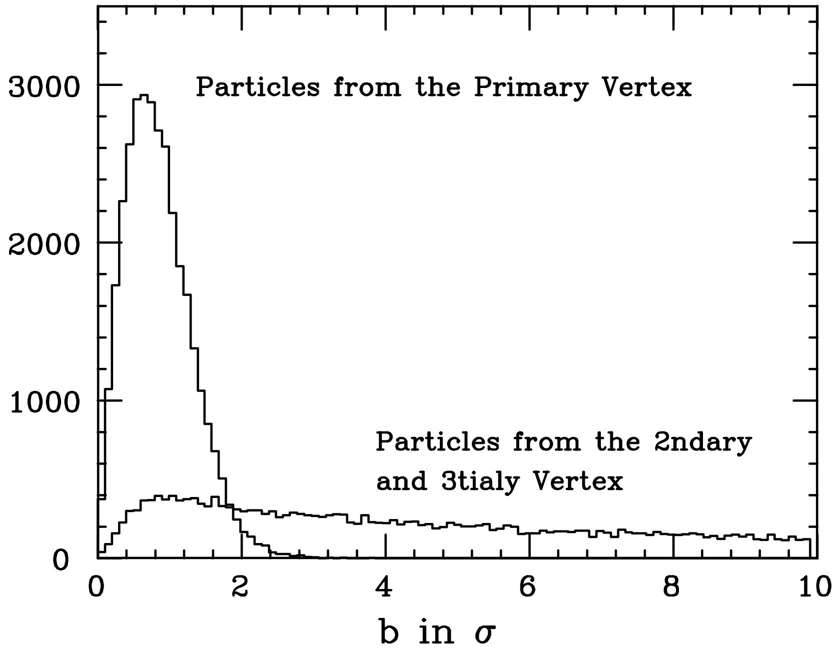

Figure 3.4: Distributions of normalized impact parameter in the three-dimensional space for the charged particles from the primary vertex and for those from the secondary and tertiary vertices.

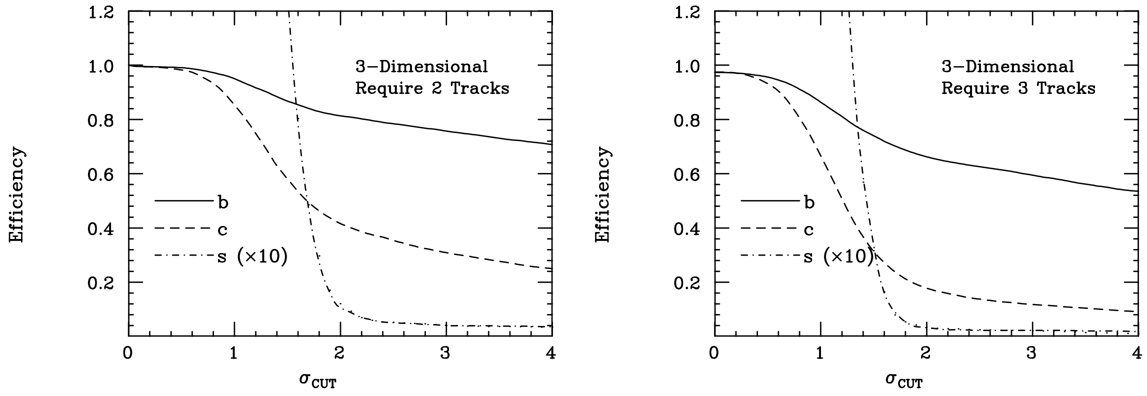

Figure 3.5: Tagging efficiency for s-, c-, and b-quark jets as functions of σ_{cut}. The curve for u jets which is not plotted here is almost same as that for s jets.

of efficiencies for two jets and the branching ratio, the suppression ratio for the background process $W \to q\bar{q}'$ becomes $\sim 1.2\ (0.27) \times 10^{-3}$ for the case of ≥ 2 (3) tracks double tag, while the efficiency for the signal process ($H \to b\bar{b}$) is ~ 62 (39)% . In the case of the intermediate mass Higgs search through the process $e^+e^- \to HZ$, with $H \to b\bar{b}$ and $Z \to l^+l^-$ or $\nu\bar{\nu}$, the main background comes from $e^+e^- \to ZZ \to l^+l^-(\nu\bar{\nu})q\bar{q}$. This background cannot be suppressed as much as in the case of W pair background because the process including $Z \to b\bar{b}$, which has a sizable branching ratio, has the same topology as the signal process. However, we don't need such stringent light quark suppression as in the case of W pair background because the cross section is not as large as the W pair production. If we require at least one jet to be identified as a b-quark jet with ≥ 2 (3) tracks having large impact parameter, the background is suppressed to 31% (24%), with a tagging efficiency of 95% (86%).

3.2.5 Background Considerations

As discussed in section 3.7.6, the beam background in linear collider experiments is quite different from that of storage ring experiments. The main background to detectors consists of photons emitted from the front surface of the final quadrupole magnet, which is bombarded by electron-positron pairs created by beam-beam interactions. These electrons/positrons themselves could be the background near the beam line as described in section 3.7.6. The spectrum of the background photons shows a broad peak around 200 keV and a sharp annihilation peak at 0.5 MeV.

A large number of the background photons flow out from the aperture of the tungsten mask. The inner layer of the VTX is exposed to direct hits from the photons and the outer layer is hit by photons scattered by inner materials including the beam pipe. If we assume that both the inner and outer layers are exposed to the photons directly as a worst case, the number of pixels hit by the background photons is

$$N_{bg} = N_p V_p \lambda I,$$

where N_p is the number of pixels (4×10^8), V_p is sensitive volume of a pixel ($= 25 \times 25 \times 50\ \mu\text{m}^3$ if the effective thickness is 50 μm), λ is the linear attenuation coefficient for photons in silicon (0.3/cm at 200 keV), and I is the intensity of the photon flux per unit area. The number of electrons/positrons hitting the final quadrupole magnet is estimated to be $\sim 5 \times 10^6$, and the number of back-scattered photons per electron/positron is ~ 1. Since the VTX is about 2 m away from the photon source (the front surface of the final quadrupole magnet), the intensity of photons at the VTX is $I = 5 \times 10^6 \times (2\pi \times 200^2)^{-1} \sim 20$. Putting those numbers into the equation, we get $N_{bg} = 75$, which is negligibly small compared with the background due to the direct hits by the electron/positron tracks.

3.3 Central Tracking Device

The central tracking device plays a crucial role, in particular, in Higgs studies, where we have assumed an ultimate momentum resolution and one-to-one matching of a calorimeter hit to a charged track in the central tracker. In addition, the central tracker has to survive the expected backgrounds from beam-beam interactions. We will demonstrate below that a small jet-cell type cylindrical drift chamber (CDC) can realize the required performance within the presently available detector technology. Brief discussions on electronics followed by cost estimation will be also given in this section.

3.3.1 Design Criteria

Momentum Resolution

The most stringent constraint on momentum resolution comes from the required missing mass resolution for lepton pairs from decays of Z^0 bosons produced in the process $e^+e^- \to Z^0h$. In order that the measurement error might be negligible compared with the beam energy spread, the momentum resolution should be better than 0.4 % for a 50 GeV track. This requirement on the momentum resolution sets the design goal for the resolution of the reciprocal transverse momentum $\kappa = 1/p_T$. If this goal is achieved, the momentum resolution is good enough for the charge separation of even 5 TeV leptons.

The κ resolution is given by $\sigma_\kappa^2 = (\sigma_\kappa^{meas})^2 + \left(\sigma_\kappa^{MS}\right)^2$, where the first term in the right-hand side is from coordinate measurement errors while the second term from multiple scattering in the chamber gas:

$$\begin{aligned} \sigma_\kappa^{meas} &\simeq \left(\frac{\alpha\sigma_x}{BL^2}\right)\sqrt{\frac{720}{n+4}} \\ \sigma_\kappa^{MS} &\simeq \left(\frac{\alpha C}{BL}\right)\sqrt{\frac{10}{7}\left(\frac{X}{X_0}\right)} \cdot \kappa \end{aligned}$$

with $\alpha = 333.56$ ($\mathrm{cm} \cdot \mathrm{T} \cdot \mathrm{GeV}^{-1}$), $C = 0.0141$ (GeV), L = lever arm length (cm), B = magnetic field (T), $\left(\frac{X}{X_0}\right)$ = thickness in radiation length, and n = the number of sampling points. We have, for instance,

$$\left(\frac{\sigma_{p_T}}{p_T}\right)^2 = (1.1 \times 10^{-4} \cdot p_T[GeV])^2 \ + \ (1.5 \times 10^{-3})^2$$

for $L = 200$ cm, $B = 2$ T, $\sigma_x = 100$ μm, $n = 100$, and $(X/X_0) = 1.1$ % when CO_2-isobutane(90/10) is used as the chamber gas. The effect of the constant term (multiple scattering) is less than 15 % on σ_κ for $p_T \geq 20$ GeV in this case. This example is already very close to our design goal.

In order to see how the interaction point (IP) constraint or the extra-coordinate information improves the momentum resolution, we have to take proper accounts of the multiple scattering. We will focus our attention on the detector configuration shown in Fig.3.6. The radiation lengths of the relevant materials are listed in Table 3.2. The IP constraint improves the momentum resolution by approximately a factor of two even in the presence of multiple scattering. If we include the Si vertex detector into track fitting, coordinate information from the Si vertex detector is equivalent to the use of the IP constraint.

Taking these into account, we fix the detector parameters as follows:$B = 2$ T, $r_{in} = 30$ cm, $r_{out} = 230$ cm, $n = 100$, and $\sigma_x = 100$ μm. Figs.3.7-a) and -b) show the polar angle dependence of the momentum resolution without and with the IP constraint, respectively. With the IP constraint, the momentum resolution obtainable with this set of detector parameters satisfies the design requirement from Higgs studies.

Cluster Track Matching

In order to get an ultimate resolution for jet invariant mass, the essential point is one-to-one matching of a calorimeter cluster and a charged track in the CDC. Since the calorimeter will exploit a Si pad detector of 1×1 cm^2, our goal is to keep the track extrapolation error reasonably below this size. The position resolution in the azimuthal direction automatically satisfies this requirement when we demand the momentum resolution required from Higgs

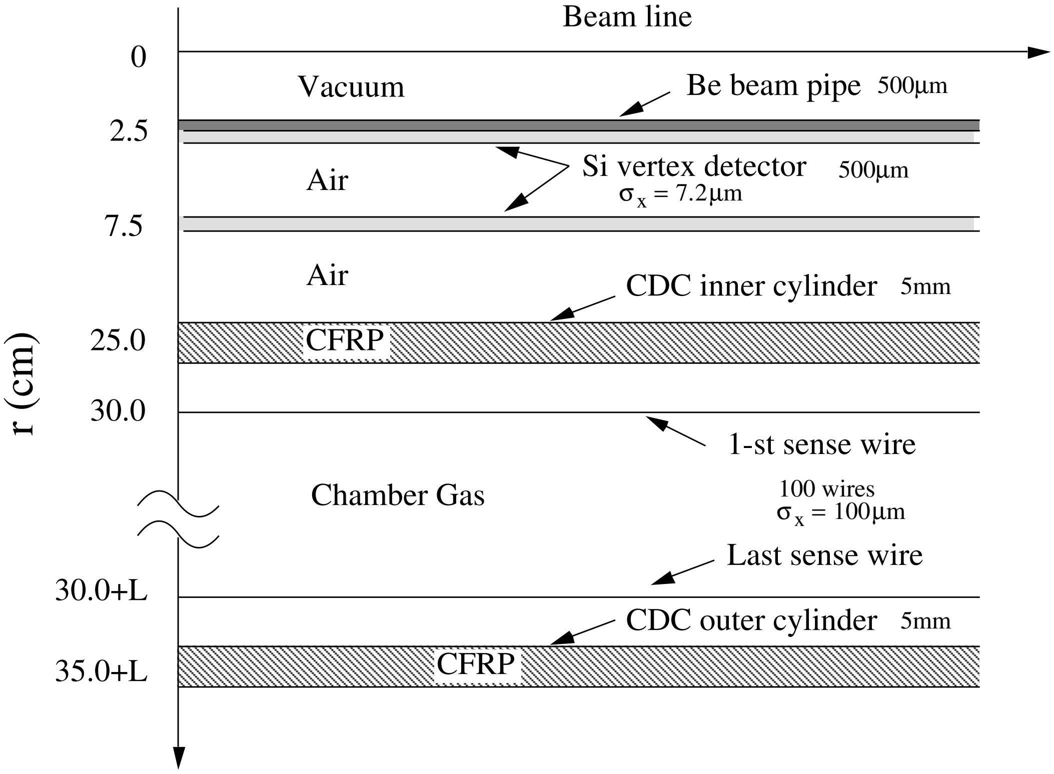

Figure 3.6: The configuration of tracking devices.

studies. Therefore, our main concern is the z-resolution at the front face of the electromagnetic section of the calorimeter. The calorimeter front face is at $r = 250$ cm and there is no massive material but the CDC's outer cylinder made of CFRP(0.5 cm) between the CDC and the barrel calorimeter.

An error matrix calculation showed that the effect of multiple scattering quickly disappears when the momentum exceeds 5 GeV and that a z-resolution of 1 mm or better can be achieved at the calorimeter front face, if seven stereo layers with $\sigma_z = 1$ mm are available.

Material	X_0^{-1}(%/cm)
Be	2.8
Si	10.7
CFRP	3.0
Air(1atm)	0.0035
CO_2/C_4H_{10}(90/10)	0.0055

Table 3.2: A list of materials and their radiation thickness per unit length.

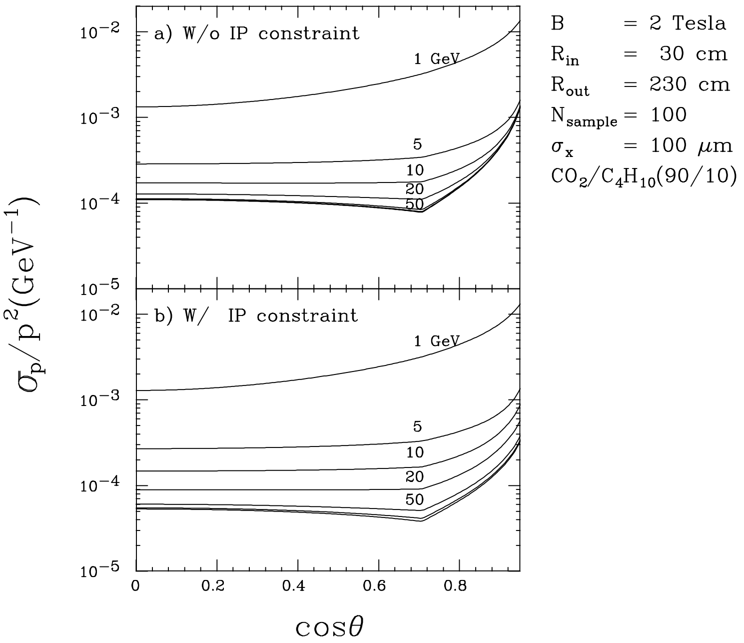

Figure 3.7: σ_p/p^2 as a function of the cosine of the polar angle: (a) without and (b) with the IP constraint. The different curves correspond to different momenta: $p = 1$, 5, 10, 20, 50, 100, and 250 GeV.

2-Track Separation

A limited capability of two-track separation (two-hit separation) is one of the most important effects to deteriorate the measured track quality. The fraction of missing hits for decay daughters from a single W boson whose momentum is 250 GeV was investigated. The cell size is assumed to be 10 cm (the maximum drift length is 5 cm). The effect of Left/Right ambiguity is also taken into account. If the two hits separated by 1 mm each other can be distinguished, only five percent of the hits are missed at the innermost layer and one percent at the outermost layer. A two-hit separation capability of 1 mm can be achieved by our CDC design. After 100 nsec (equivalent to a 1 mm drift) from the arrival of the first electron, the pulse height become about one half of the peak so it is easy to separate two hits whose distance is greater than 1 mm.

Self T_0 determination

Since the JLC beam has a multi-bunch structure, each hit has its own T_0 depending on which bunch makes the hit. The CDC should have self-T_0 determination capability. The T_0 determination can be done as follows: the drift distances are given as a function of one hundred discrete values of T_0's. After track finding, the T_0 is determined to give a minimum χ^2 in circle-fit of the track. To meet the requirement of a spatial resolution of 100 μm with a drift velocity of 10 μm/nsec, the timing resolution should be 10 ns for each hit. Thus one can expect a 1.0 ns timing resolution for one track which has 100 hit points. Adjacent beam bunches locate 2.8 standard-deviation away from the bunch which has an event. The track-based T_0 determination can be done easily.

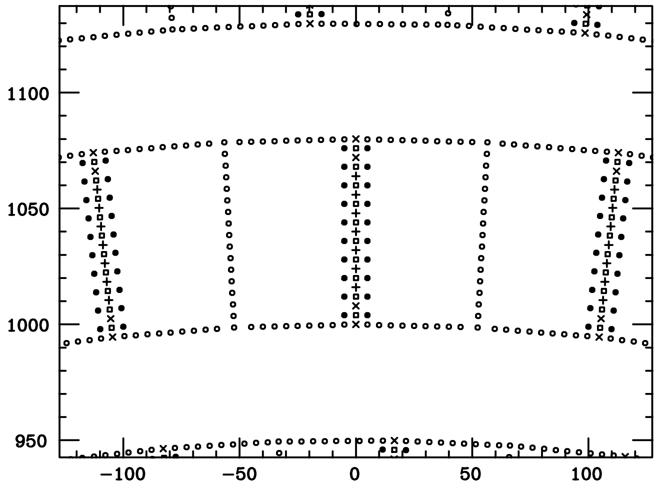

Figure 3.8: The basic cell structure.

Backgrounds

i) Soft photon background

The primary background electrons and positrons are produced through coherent and incoherent QED processes. They hit the wall of the mask and produce a lot of photons as the secondary background[1]. The energy spectrum of these photons has a broad peak near 100 keV and a narrow steep peak at 500keV from annhilation. The total number of the primary electrons produced at a beam crossing and hitting on the outer surface of the mask is at most 10^4 at center-of-mass energy of 500 $/rmGeV$. Since the conversion ratio of the primary electron to the secondary photon is about one, 10^4 photons come into the CDC volume. 2.5 photons are scattered off in each 1cm sampling thickness by the chamber gas and 1.3 photons from wires in one superlayer. The expected background hit per sense wire is 0.06 at the innermost layer and less than 0.01 at the outermost layer. The tracking can be done under these photon backgrounds.

ii) Mini-jet background

It is pointed out that two-photon induced hadronic events, so called "mini-jets", can be a background at the JLC[2]. At a center-of-mass energy of 500 GeV, the mean value of total energy of mini-jet within the CDC acceptance is expected to be 2.5 GeV and charged multiplicity is about five[3]. The number of mini-jets whose transverse momentum is greater than 1 GeV is estimated to be $1 \sim 20$ jets at one beam crossing for c-band case. Since the CDC can distinguish the tracks from different bunches, the mini-jet cannot be a problem. Even if the mini-jet ratio is, as the worst case, ten jets a beam crossing, the probability that at least one mini-jet overlapping the real event in the same bunch is 9.6%.

3.3.2 Chamber Geometry and Cell Structure

As shown in the previous subsection, a small cell type cylindrical jet chamber can realize the required performance. Details of the CDC structure are given in this subsection.

The super layer structure allows to find a track segment as a vector hit in each super layer. The number of super layers is calculated from the thickness of one super layer (8 cm), the thickness of gap between adjacent super layers (5 cm), and the lever arm length (200 cm). The gap between super layers is determined by the stereo angle. We can get 15 super layers in the CDC: 8 axial layers and 7 stereo layers. Stereo angle is set to be 100 mrad to give $\sigma_z = 1$ mm per superlayer.

The basic cell structure is shown in Fig.3.8. One jet-cell has 7 sense wires of $30\mu m\phi$ tungsten. Maximum drift length is 5cm. They are strung with 8mm spacing and are applied +2.5kV. The outermost two wires and innermost two wires are dummy sense wires and their voltage is 1.8kV. Between sense wires,a potential wire is strung and is grounded. The grid wires are placed at 5mm away from the sense wire plane. Their voltage is set to be -0.5kV. The grid wires allow us to make good equi-drift time shape and to minimize a sence wire displacement due to electric force from adjacent layers. All wires except for the active sense wires are $150\mu m\phi$ alminum wires to reduce total wire tension. Sense wire planes are staggered not to align any two sense wire planes on the same radial line.

Using an electric field calculation program, we studied the basic charactaristics of this wire configuration with chamber gas of CO_2-isobutane(90:10). The Lorentz angle of this gas is about 15 degrees. Fig.3.9 shows the equi-drift time map. The calculation shows that about ten electrons arrive at the sense wire within a first time bin whose width is 5 nsec. This suggests that if the threshold is set at a few electrons, the required timing resolution (100ns) can be achieved.

Since the CDC is 4.6 m long in z-direction, gravitational sagging is not negligible. To minimize total sagging from gravitational and electro-static forces, we set the tension of sense wires at 145 gw and that of other wires at 500 gw to equalize the gravitational sagging of all the wires (250 μm). The displacement of sense wires from their nominal positions due to electro-static force is calculated to be from 25 to 54 μm assuming massless wires in the multi-cell configuration. The accuracy in machining of the chamber endplate is 10 μm.

The total number of jet-cells is 1200 and the total number of wires is 115000. The total wire tension is 50 tons, which is tolerable for the following mechanical structure. To support the total wire tension, the outer cylinder is made of CFRP of 5 mm thickness and end-plates are made of aluminum of 25 mm thickness. When the end-plates are supported by the outer cylinder only, the displacement at the inner edge of the end-plate is estimated to be 8 mm.

3.3.3 Readout Electronics

The central tracking device should have good spatial resolution and two-track separation capability in a multi-hit environment. Also fairly good resolution on the charges of the ionization pulses is required to have rough z-coordinate information by the charge division method.

To meet these requirements, slow repetetion rate of the JLC ($\sim$ 200 Hz) allows the use of waveform sampler (Flash ADC), which logs the whole time developement of the drift chamber signal. The chamber signal will be readout from the both ends of sense wires.

Output from amplifiers will be fed to Flash ADC's with 12 bits for energy bin and 1024 time bins clocked at the rate of 200 MHz, i.e. total time window of 5 μs with a time slice of 5 ns. The conceptual block diagram is shown in fig.3.10.

Making use of the full information on the waveform, accurate determination of the arrival time is possible by the double threshold leading edge method[4]. The time resolution will be a fraction of the time slice of the sampling, hence the contribution on the spatial resolution of $\sim 20\mu$m from the electronics systyem is expected in our case. By sampling the whole waveform, we can also get the drift time and the charge of the the multiple hits, even if we have the later

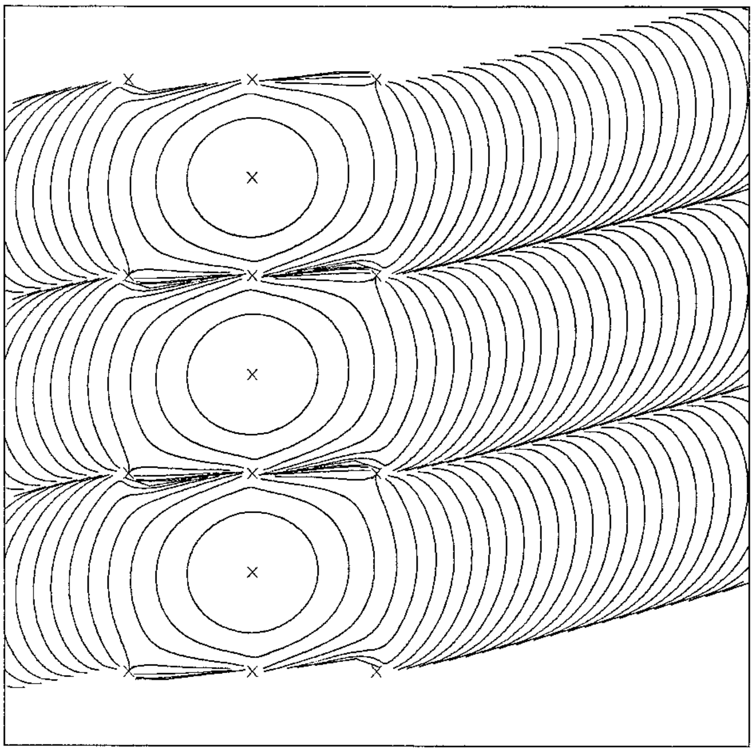

Figure 3.9: Equi-drift time map.

one overlapped with the tail of the first pulse. This is essential to the efficient tracking in the multi-hit environment.

3.4 Calorimeter

3.4.1 Design Criteria

Our primary purpose at the first stage of the JLC experiment is to detect the intermediate mass Higgs boson if it exists. Such a Higgs boson should be produced by Z^0 associated processes at JLC energies, and can be most clearly detected when the Z^0 boson is identified through its leptonic decay into electrons or muons. Although the branching fractions of these decay modes sum up to only 7%, the good momentum resolution of charged leptons measured by the CDC is of great help in identifying the Higgs boson as a recoiling system of these lepton pairs. Other decay modes of the Z^0 boson have larger branching fractions: quark pair decays have about 70 % branching fraction and neutrino modes have about 20 %. If we can make use of these decay modes, the intermediate mass Higgs boson can be discovered evev if the luminosity of the JLC is not as large as expected.

In the absence of charged lepton pairs in the final state of the Z^0H^0 process, the mass of the Higgs boson should be solely reconstructed from the invariant mass of the dijet with b-quark flavors. With the help of b-flavor tagging by the vertex detector, background events from W^+W^- pair production process can be greatly suppressed and practically can be ignored. The most significant background for the hadronic detection of the intermediate mass Higgs boson come from the Z^0Z^0 pair production process, resulting in four hadronic jet or two hadronic

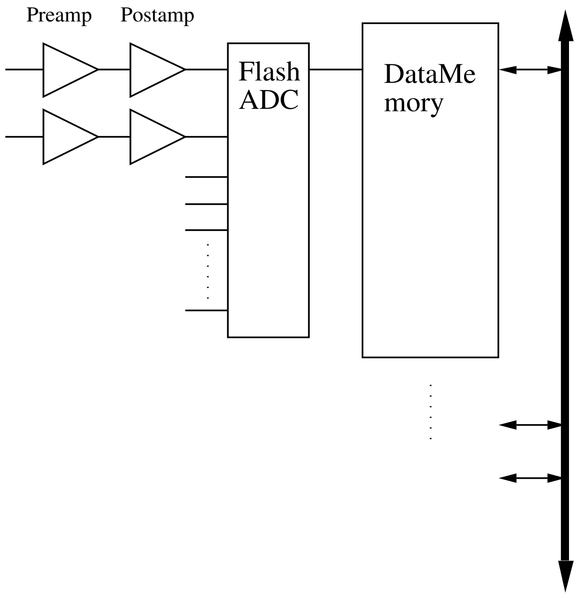

Figure 3.10: Schematic diagram of waveform sampling.

jet final states. Especially good jet-invariant mass resolution is required in order to separate reconstructed Higgs bosons from background Z^0 bosons in this mass region of the Higgs.

Detector induced effects on the dijet invariant mass resolution include:

- calorimeter segmentation,
- calorimeter energy resolution and
- nonlinearity of the hadron calorimeter.

The calorimeter segmentation is closely related to the position resolution of reconstructed hadronic and electromagnetic clusters and to the separation of two detected clusters. If we can measure the position of the hadronic clusters precisely, and separate two nearby hadronic clusters inside hadronic jets, then charged particles detected in the central tracking chamber can be correctly connected to these clusters. Precisely measured momenta of these particles by the CDC will greatly improve the invariant mass resolution of the dijet.

We have studied the dijet invariant mass resolution of our detector. We assumed a calorimeter based on interspersed scintillator plates and Pb absorber plates. Its inner surface is located at 2.5 m in radiusand is about 6 m long. The first 40 layers form the electromagnetic calorimeter (ECAL) and the remaining layers form the hadronic calorimeter (HCAL). In order to measure shower position precisely, Si pads of $1 \times 1\text{cm}^2$ are put into ECAL at a depth of 4.3 radiation length, which provide a position measurement of about 3 mm resolution. Each calorimeter wedge contains four ECAL towers of about $10 \times 10\text{cm}^2$ at the inner surface of the barrel part and one HCAL tower of about $20 \times 20\text{cm}^2$ at its innermost surface. The energy resolutions of these modules are assumed to be:

$$\begin{aligned} \sigma_E/E &= 15\%/\sqrt{E} \oplus 1\% \text{ for ECAL and} \\ \sigma_E/E &= 40\%/\sqrt{E} \oplus 2\% \text{ for HCAL.} \end{aligned}$$

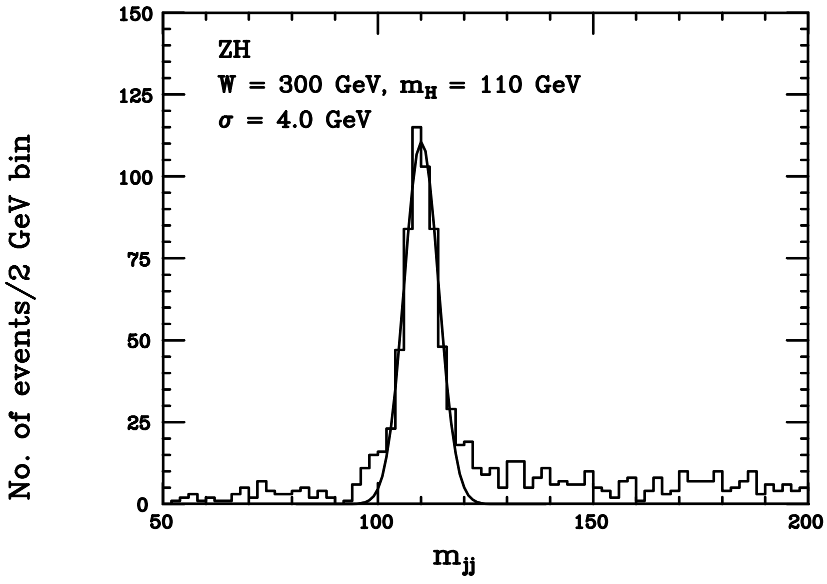

Figure 3.11: Jet mass resolution for Higgs

In Fig. 3.11, we present the result of a calculation of the dijet mass resolution for our model calorimeter. We can get reasonably good jet mass resolution with the assumed detector. A design of the calorimeter which can achieve the assumed performance is described in the following subsections.

3.4.2 Detector Configuration

In order to achieve good hadron energy resolution, a compensated lead/plastic scintillator(PMMA) sandwich calorimeter scheme is adopted. It consists of a fine-sampling ECAL of 29 radiation lengths, a coarse-sampling HCAL of 5.6 interaction lengths, and a silicon pad detector located behind the first $4.3X_0$ of the ECAL. The schematic view of the calorimeter assembly is shown in Fig. 3.1. The whole calorimeter is placed inside the solenoid to achieve good energy resolution and hermeticity. It has a tower structure and each tower nearly points to the interaction point.

The ECAL consists of 40 layers of 4mm thick lead plates and 40 layers of 1mm thick PMMA plates. Its thickness is chosen to contain 250 GeV electron shower. According to simulations[5], this configuration is expected to give a stochastic term for the energy resolution of

$$\sigma_E/E = 15\%/\sqrt{E} \oplus 1\% \tag{3.1}$$

for EM showers, where a constant term of 1% is assumed. Beam test results by ZEUS[6] and SPACAL[7] also support this estimation for the stochastic term, while the constant term of 1% is a bit of a challenge. The segment size is 10cm × 10cm, which is too big to calculate the shower center position from the energy deposit distribution over different segments. Instead, a silicon pad detector is installed. This is described later. The particle densities of reactions are thin enough to avoid multiple neutral particles coming into one segment.

The HCAL consists of 8mm thick lead plates and 2mm thick PMMA plates. The total thickness is 120cm (5.6 interaction length) which is limited by the available space and by mechanical strength. The ECAL and HCAL give 6.5 interaction lengths in total, which is thick enough to contain 98% of a 20GeV pion's energy and 95% of a 200GeV pion's energy. This configuration is expected to achieve an energy resolution of

$$\sigma_E/E = 40\%/\sqrt{E} \oplus 2\% \tag{3.2}$$

for hadrons, extrapolated from the results of SPACAL[7]. The segment size is 20cm × 20cm and one segment contains 75% of the energy of a 10GeV pion shower when it is injected at the center of the segment[6].

Photons from the scintillator are collected by wave length shifter plates (WLS) located on both sides of the scintillator plates of the HCAL, and at one side of those of ECAL. Position dependence of the light output is corrected using the silicon pad information. The WLS's extend to the bottom of the tower, and photo-diodes are attached at the ends to read out the photons. About 2000 photo-electrons are expected to be obtained as an output of the photo-diode for a 1GeV shower. The noise level of the preamp is about 700 electrons (FWHM) equivalent if typical photo-diodes are used, which corresponds to about 300MeV. This noise level is a little too high, and APD's or forth-coming devices like VLPC or image intensifier+CCD may be needed[9]. In order to avoid the WLS walls pointing to the interaction point, the tower projection has a little offset in both the θ and ϕ directions.

A silicon pad detector (Si-pad) is located after the first $4.3X_0$ of the ECAL. A pad size of 1cm × 1cm is presently assumed, and this achieves a position resolution of about 3mm. This good position resolution is necessary for track-cluster matching. Excellent two-cluster recognition can also be achieved, and these help to identify particles and to assign the correct energy to photons when photons overlap charged particles. The pads give a signal of 16000 electrons for minimum ionizing particles, and can separate e, μ and π in combination with ECAL and HCAL energy information. The system is expected to achieve a pion rejection factor of about 1/50 for an electron efficiency of 90%[8].

3.4.3 Mechanical Structure

Calorimeter towers are assembled to the whole detector as shown in Fig. 3.1. The barrel part has an inner radius of 2.5m, the outer radius of 4.0m, and the length of 6m, and it consists of 2500 towers. Each tower weighs about 600kg, and the total weight of the barrel part is about 1500 tons. This weight is supported by a half-cylinder with negligible deformation as shown in Fig. 3.12. The towers are first attached to a ring, and the rings are then placed on the support cylinder. During the tower construction, it stands vertically while lead and scintillator plates are stacked. In order to attach the towers to a ring, the towers must have a self-supporting structure so that we can lay them horizontally to attach them to the ring structure. This can be achieved by mounting each component in a box made of 2mm thick stainless steel as shown in Fig. 3.13. This simple structure can hold the weight of 600kg with a maximum displacement of 1mm at the front face of the tower even when the tower is held horizontally and fixed at the bottom end only. After attaching them to the ring, each ring is put on the supporting cylinder, slidden inward, and fixed at the design location. The half-cylinder is made of 10cm thick stainless steel and is supported by the iron structure. The solenoid is divided into three pieces as shown in Fig. 3.1 to support the cylinder not only at both ends but also at two additional points between the ends. This four-point support has a maximum deformation of only 10μm at the center of the cylinder, while a several millimeter deformation is introduced if the cylinder is supported only at both ends.

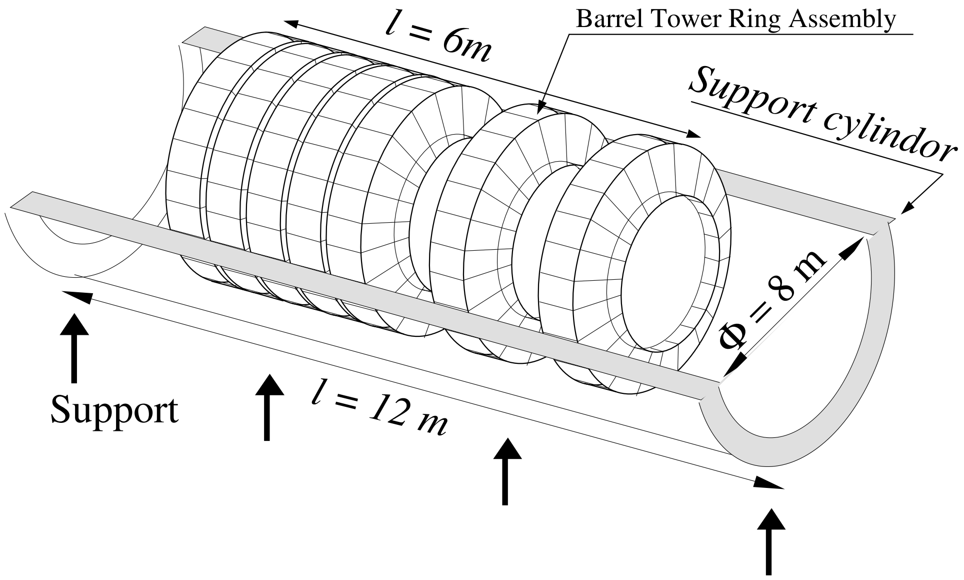

Figure 3.12: Schematical view of the calorimeter assembly

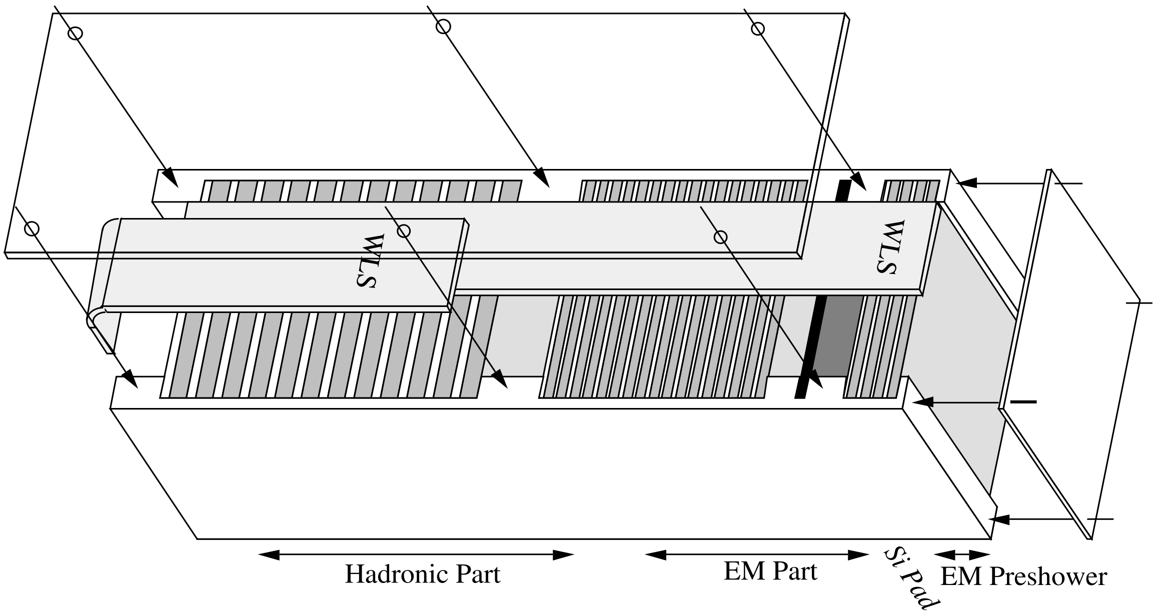

Figure 3.13: Schematical view of the calorimeter tower

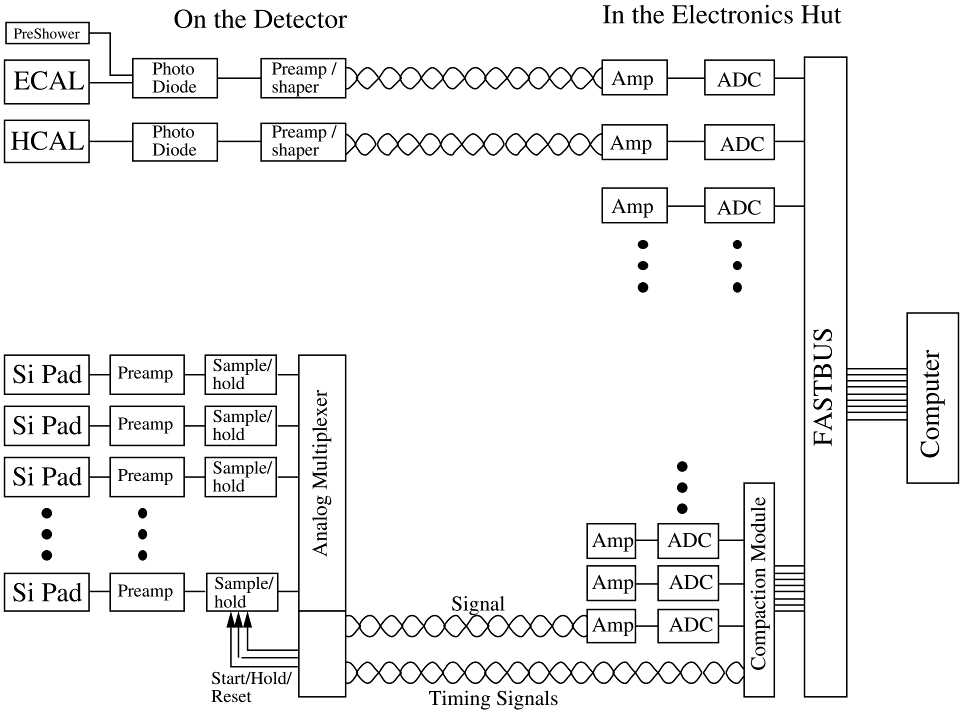

Figure 3.14: Layout of DAQ system

Each endcap calorimeter assembly has an outer radius of 4m, an inner radius of 0.35m, and a thickness of 1.5m. It has a tower structure similar to the barrel part. Each endcap calorimeter consists of about 1250 towers and weighs about 640 tons.

3.4.4 Electronics

Photons from the scintillators are collected by WLS's and are read out by photo-diodes because the whole calorimeter is placed in the magnetic field. Low noise preamps are located in each tower. The capacitances of both the photo-diodes and the Si-pads are about 80pF, which gives a noise level of $\sim$ 700 electrons (FWHM). The dynamic range of the signal is from $\sim$ 100 MeV (well below the MIP signal on ECAL) to $\sim$ 250GeV (Bhabha electron energy at $\sqrt{S} =$ 0.5TeV), which can be measured with a standard bi-linear 12bit ADC. The number of channels for ECAL and HCAL is only 20k and 5k, respectively. Thus the calorimeter signals are easily delivered to the electronics hut, amplified, and read out with a conventional FASTBUS ADC system as shown in Fig. 3.14.

The Si-pad detector has 2×10^6 channels in total, and to read out these signals is not trivial. To lay down two million cables from the detector to the electronics hut is not a practical solution. Thus we will install an analog multiplexer in each tower and transmit 400 channels of data serially to the electronics hut. These data are pedestal-suppressed by compaction modules and read out through FASTBUS.

3.5 Muon Detector

3.5.1 Design Criteria

The requirements for the muon detector are rather simple because it need not measure the momentum of muons, it simply needs to tag muons.

Since the CDC has very good momentum resolution, the muon momentum is known very precisely once a matching between a CDC track and muon detector hits is successfully made. For this purpose, many position measurements along the muon track are essential, while the resolution of each position measurement is not so important. Timing measurements are also needed to reject cosmic ray muons. Modest timing resolution can reject cosmic ray muons effectively since the duty factor of the data taking is very low.

Muons are usually the cleanest signal in a search for new particles, and we must minimize the region which is not sensitive to muons.

3.5.2 Detector Configuration

The muon detector consists of six super-layers of single-cell drift chambers and one layer of plastic scintillation counters as shown in Fig 3.15.

In the case of the barrel part, the innermost and outermost super-layers are located inside and outside of the flux return yoke, respectively, and have four layers with xx'yy' wire configuration to measure both ϕ and z coordinates. The remaining four super-layers are interleaved between the yokes and have two layers with an xx' configuration to measure the ϕ location only. Each layer consists of a single-cell drift chamber with a cell size of 10cm $\times$ 5cm and a wire length of 10m. A wire support is located at the middle of the wire to reduce the wire sag. Using 100μm ϕ tungsten wire with 600g wire tension introduces a sag of $\sim$ 450 μm, and this dominates the position resolution of the chamber.

The endcap muon detector has a super-layer configuration similar to the barrel part except that two interleaved super-layers have an xx' configuration while the other two have yy'. The wire lengths differ according to the location and the length of the longest wire is 15m, which needs two mid-supports.

The total number of channels is 7700 for the barrel part and 2400 for each endcap part. These can easily be sent to the electronics hut and read out with conventional TDC's.

3.5.3 Expected Performance

The position resolution of each interleaved layer is about $\sim$ 500 μm, which is dominated by the wire sag. Once the z-coordinate of the hit is determined, the resolution can be improved by making a wire-sag correction. However, 500μm resolution is good enough to identify muons. The innermost and outermost super-layers can achieve much better position resolution by themselves because they have both z and ϕ measurements.

Muons must have a momentum of at least 3.5GeV/c to be identified as a muon by the muon detector. This is due to the large energy loss of $\sim$ 2GeV by the calorimeter.

The polar angle coverage of $\mid cos\theta \mid < 0.99$ is achieved without any insensitive region. A detection efficiency better then 99% can be achieved over this polar angle range.

The effect of the background muons from the beam line has not yet been studied in detail, but we expect that magnets can effectively sweep out these background muons as will be

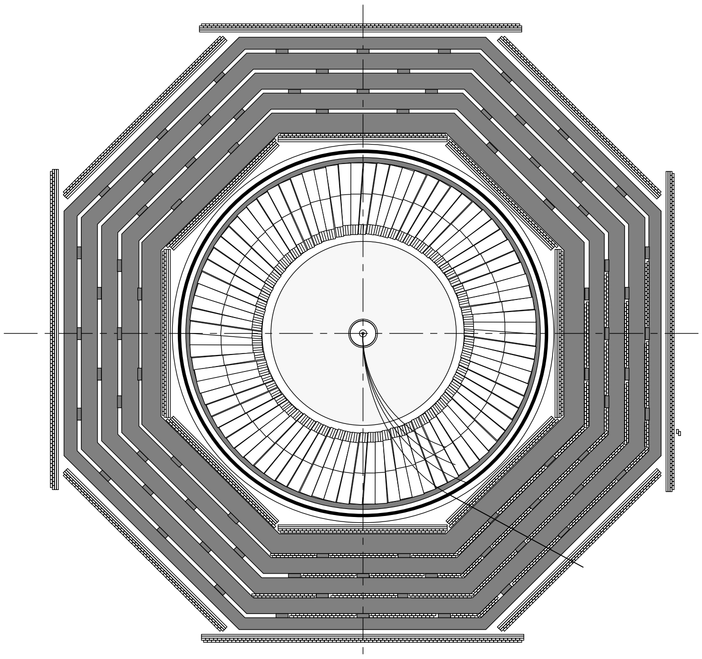

Figure 3.15: Layout of the muon detector.

described in section 4.7.

3.6 Superconducting Solenoid Magnet

3.6.1 General Characteristics

We require that the superconducting solenoid magnet is placed outside the calorimeter to achieve good hermeticity. The solenoid magnet has a structure shown in Fig. 3.16 and parameters listed in Table 3.3. The bore diameter is 9 m and the overall length is 10 m. To simplify the assembly procedure and also to provide a rigid support for the carolimeter, we divide the magnet into three parts. Each part is 2.6 m in length and is equipped with its own separate cryostat. The central part and both of the end parts consist, respectively, of 257 and 278 turns of double layer coaxial coil windings. This configuration is to compensate the field drop along the beam axis.

The superconducting magnet requires a relatively thick iron yoke to ensure the 2 Tesla uniform field in the central tracking region. In order to keep the maximum field in the iron yoke below 2 Tesla, we need a total amount of 11,500 tons of iron. The flux line distribution is shown in Fig. 3.17, where the magnetic field uniformity in the tracking region is better than ± 0.6 % of the central field.

The overall inductance of the magnet is 5.5 H. Consequently, the total stored energy is 1.1 GJ, when the magnet is operated at 20 kA to produce the 2 tesla central field.

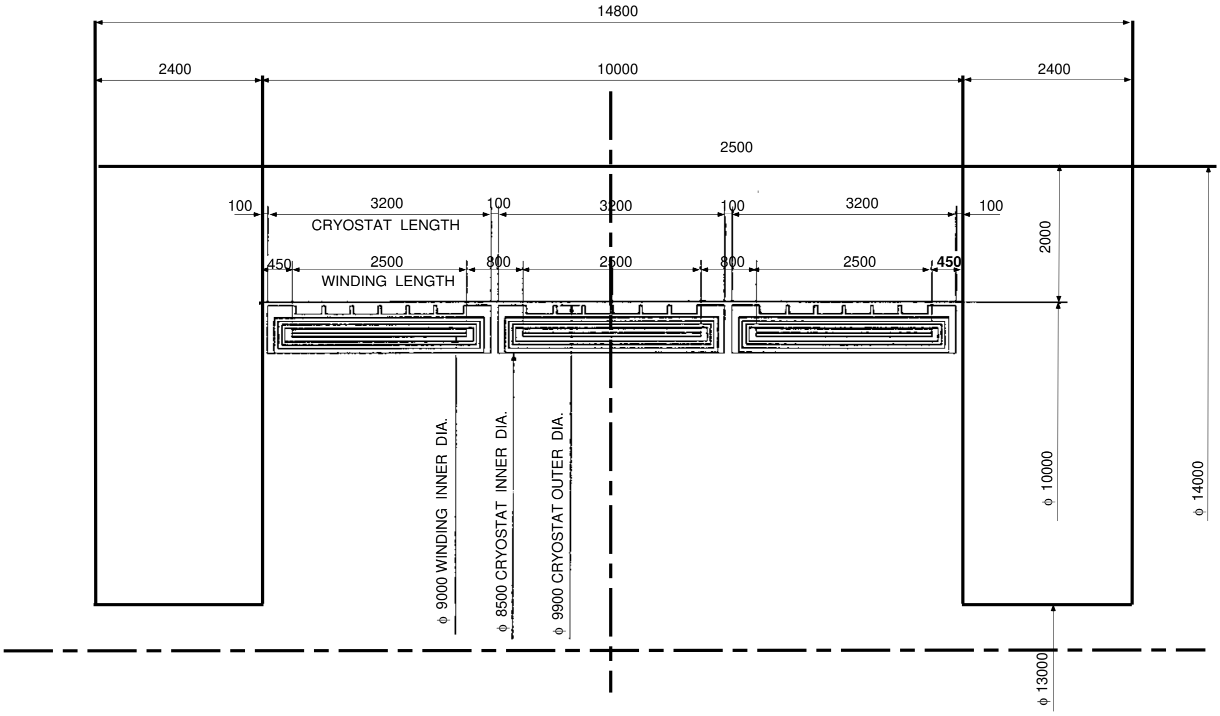

Figure 3.16: Configuration of the solenoid magnet

Coil bore diameter	9	(m)
Total length	10	(m)
Inner diameter of the cryostat	8.5	(m)
Outer diameter of the cryostat	9.9	(m)
Number of modules	3	
Operation current (2Tesla)	20,000	(A)
Inductance	5.5	(H)
Stored energy	1.1	(GJ)
Refrigeration load at 4.2K	330	(W)
Weight of the conductor of each module	52	(tons)
Total weight of the conductor	151	(tons)
Weight of one piece of the coil	120	(tons)
Magnet weight without iron	720	(tons)
Conductor length of each module	8.0	(km)
Total conductor length	24	(km)
Total weight of the magnet with iron	12,000	(tons)

Table 3.3: Parameters of the superconducting solenoid

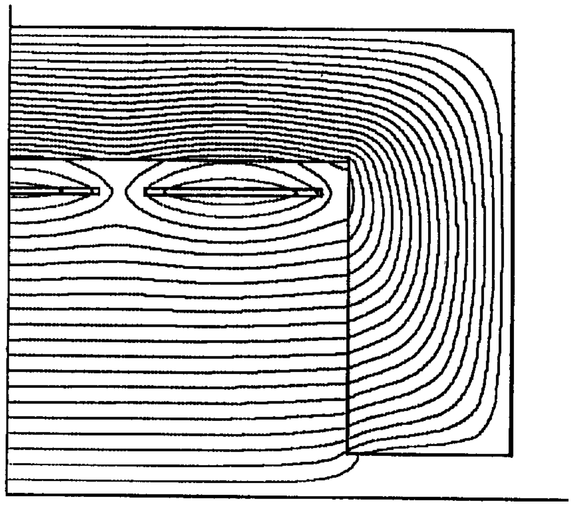

Figure 3.17: Flux line distribution

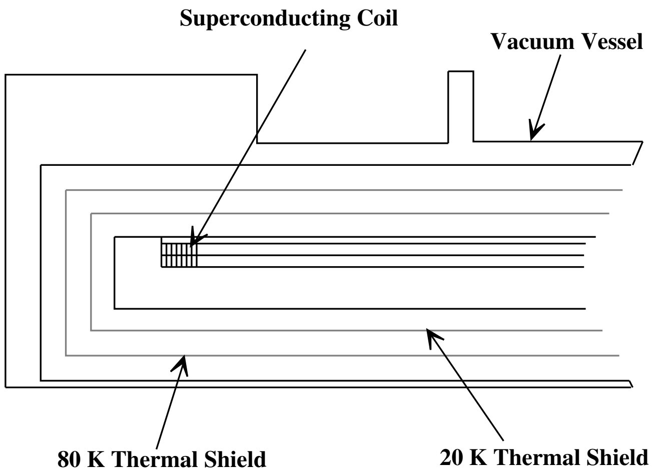

Figure 3.18: Cryostat of the solenoid

3.6.2 Cooling System

There are two reliable cooling methods: the conventional pool boiling and the cooling by the flow of two-phase helium that has a large heat capacity owing to the latent heat at the low temperature. The JLC detector magnet needs approximately 15,000 liters of liquid helium, when cooled by a pool boiling system. Such a large volume of liquid helium cannot be brought back to its circulator, when the magnet gets quenched. We are forced to release the resultant helium gas to the atmosphere. The duct system to make it possible is impractical, since the experimental hall is expected to be in deep underground. Therefore, it is absolutely necessary to reduce the amount of the liquid helium in view of safety.

This can be achieved by a direct cooling system employing the flow of two-phase helium through a cooling path in the conductor. The required amount of the liquid helium in this system is about 500 liters, which is 1/30 of that required by a pool boiling system.

The cryostat for this magnet is shown in Fig. 3.18. The cryostat is a vacuum chamber with superinsulation. The two shields covering the coil are kept at 20 K and 80 K, respectively, by the helium gas from the refrigerator. The 20 K shield is essential to help further reduce the

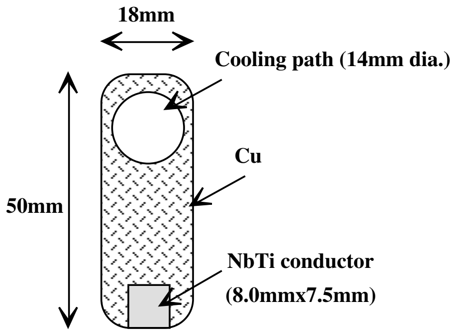

Figure 3.19: Cross section of the superconductor

Dimensions	50×18	(mm^2)
Length of one piece	800	(m)
Diameter of the cooling path	14	(mm)
Critical current at 4.2K in 2Tesla	50,000	(A)
Superconductor	Nb-Ti	
Ni-Ti:Cu	1:2	
Nb-Ti:Cu overall	1:36	
Number of filaments	10200	
Diameter of filament	50	(μm)
Stabilizer	Cu	

Table 3.4: Parameters of the superconductor

helium amount by controlling the pressure drop to less than 0.2 kg/cm^2.

The total heat load at 4.2 K is estimated to be 330 W. Therefore, a medium class refrigerator with a cooling power of 500 W (corresponding to electric power consumption of 500 kW) is enough to operate the magnet.

3.6.3 Superconductor

The coil is made of a Nb-Ti/Cu multifilamentary superconducting composite. The Cu/SC ratio is chosen to be 2.0 for easy mechanical handling. A cross-sectional view of the conductor is given in Fig. 3.19 and the main parameters of the superconductor are listed in Table 3.4. The operation current and the temperature are 20 kA and 5.0 K, assuming that the helium pressure at the inlet is 0.3 kg/cm^2 and the local temperature rise is 0.5 K. On the other hand, the critical current of the conductor is 40 kA at 5.0 K in a 3 Tesla field (50 kA at 4.2 K in the same field). The stabilizer of the conductor is made of Cu and the current density of this Cu part is 25 A/mm^2 when the magnet gets quenched. This current density is low enough to keep the local maximum temperature rise less than 80K, so that the magnet is safe from local mechanical stress.

3.6.4 Energy Extraction

The stored energy has to be safely extracted, on encounter with a quench. In our magnet design, all of the three modules are connected to a single dump resistor of 0.1 Ω, which absorbs all of their stored energy, even when only one of them gets quenched. This ia to avoid unbalanced force between the coils and the iron yoke. The maximum voltage at the energy extraction is 2 kV between the current leads.

3.7 Background and Masking System

3.7.1 Introduction

Three types of background problems have to be considered for the experiment at JLC-I. They are (a) high energy muons that are produced through electromagnetic interactions between the incoming beam and collimating materials in the upstream collimation section, (b) synchrotron radiations emitted by the beam when it traverses through the beam line magnets, particularly the final focus lens, and (c) e^+e^- pairs created in beam-beam collision at interaction point(IP).

Collision parameters are optimized to minimize these backgrounds while a luminosity is kept to be maximal value. The masking system in the interaction region is carefully designed to minimize such e^+e^- pair background and synchrotron radiation photons. We developed a design where the photons would not enter the active detector volume unless they are emitted by electrons/positrons beyond transverse offsets of $\pm 6\sigma_x$ or $\pm 35\sigma_y$ which are the nominal values of our collimation scheme. Here the σ_x and σ_y denote the size of the design emittance beam. In this calculation the beam is assumed to have a bi-Gaussian transverse distribution up to $\pm 3\sigma_{x(y)}$, followed by a 1 % flat tail beyond it.

Should synchrotron radiation backgrounds turn out be unacceptably large in the real life, two possibilities have to be examined: (1) the core emittance of the beam is too large, or (2) the lateral tail spread of the beam is too large. In case of (1), if the emittance cannot be rapidly improved, the experiment may be run by increasing $\beta^\star$, thus by reducing the lateral spread of synchrotron radiations at IP. In case of (2), if the reduction of beam tails turns out to be difficult, we need to resort to some beam collimation. It should be pointed out that the causes (1) and (2) are likely to occur (if they do) simultaneously. Hence the counter measures will have to be a combination of emittance improvement, optics retuning, beam tail reduction, beam collimation and others.

With beam collimation with metallic slits we create a possibility of high energy muon productions. Such muons can travel along the downstream beam line and penetrate the detector longitudinally, leaving huge energy deposits in the calorimeter and elsewhere. They can cause serious problems in the trigger and data analysis. The flux of muons depends on the tightness of the collimation as well as presence of downstream beam line components. For this reason an excessive beam collimation could turn out to be counter-productive. It should be used with a care, to reduce production of secondary tails off the collimation materials as well as to avoid an emittance growth due to collimator wake fields.

In subsequent sections we describe our strategies on how to handle those backgrounds.

3.7.2 Muons

It is difficult to estimate how many muons will be created in the collimation section since we do not know the mechanism to create a beam tail. Of course there is no muon background problem with no tail, *i.e.* gaussian beam. Total number of muons(N_μ) per electron are calculated as a function of incident electron energy(E_e) by MUON89[10] code and it is approximately expressed as,

$$N_\mu = 3.9(2.3) \cdot 10^{-4} \cdot E_e(\mathrm{GeV})/250 \quad \text{for} \quad \mathrm{E}_\mu > 2(5)\mathrm{GeV}. \tag{3.3}$$

The muons may be created as many as $2.8(1.7) \cdot 10^6$ because of $N_\mu \cdot 72$ (bunches/train) $\cdot$ 10^{10} (e's/bunch) $\cdot\, 10^{-2}$(1% tail). Typical scattering angle of muon (θ_μ) is m_μ/E_μ, *i.e.* $\theta_\mu = 1$ mrad for $E_\mu = 100$ GeV. Since a distance between a collimator and IP is about 1 km, these muons are spread over detector. Low energy muons($E_\mu <$ a few GeV) can be easily absorbed in concrete of 10 m thickness. In order to control them JLC-I has a collimation section in the final focus system. It comprises a collimator(30 radiation length), a muon attenuator[11] and "big bending" magnet(~ 15 mrad).

The penetrating probability after a collimator is mainly come from an edge scattering and it has been calculated to be 10^{-4} by R.Nelson[13]. Our collimation scheme employs "twice" collimation, that is, the beam is collimated twice at least in its phase space(x, x', y, y' and energy). Therefore no sizable tail is expected downstream the collimation section. The probability of repopulation in a tail is also estimated to be $10^{-7}/n^2$ per 1km beam line with the vacuum of 10^{-10} torr, where n is the position ($n\sigma_{x(y)}$) of the repopulation, provided that the repopulation is due to Coulomb scattering between electron/positron and residual gas ion(CO)[14]. In our case of $\pm 6\sigma_x$ of the collimation and about 1km between the collimation and IP, the probability is less than $3 \cdot 10^{-9}$. The corresponding number of particles in the tails is $3 \cdot 10^3$/train at most , which is acceptable. The detailed description of the collimation section is found in "Final Focus System" of this proposal. It should be stressed that high vacuum ($< 10^{-10}$ torr) is highly desired in final focus system in order to avoid scatterings of tail particles at QC1 pole tips *etc.* as well as synchrotron radiations .

The principle idea of muon attenuation is to confine muons inside iron pipe which has two axial magnetic fields of 1 Tesla in opposite directions corresponding to μ^+'s and μ^-'s, then simultaneously absorb muons[12]. The length of the muon attenuator is mainly determined by muon ranges and it is about 100 m at most, where muon range in iron is 56(98) m for E_μ=100(200) GeV[15]. With this scheme there is expected to be negligibly small number of muons at IP.

3.7.3 Synchrotron Radiations

A. Last Bending Magnet

Since the last bending magnet is located at 117.4 m from IP and its total bending angle is 0.55 mrad, synchrotron radiations are horizontally spread up to 6.4 cm at IP. The critical energy is about 1 MeV and the intensity is almost same as the beam intensity (O(10^{12})/train). As a half aperture of final quadrupole magnet QC1 is 0.67 cm, it is necessary to shield the synchrotron radiations. For this purpose a mask is installed at 61 m from the last bending magnet, near QC3. The mask can be made by 21cm long tungsten which corresponds to 20λ ($2 \cdot 10^{-9}$ attenuation) for a few MeV photons. Since its minimum (half) aperture is 0.3 cm

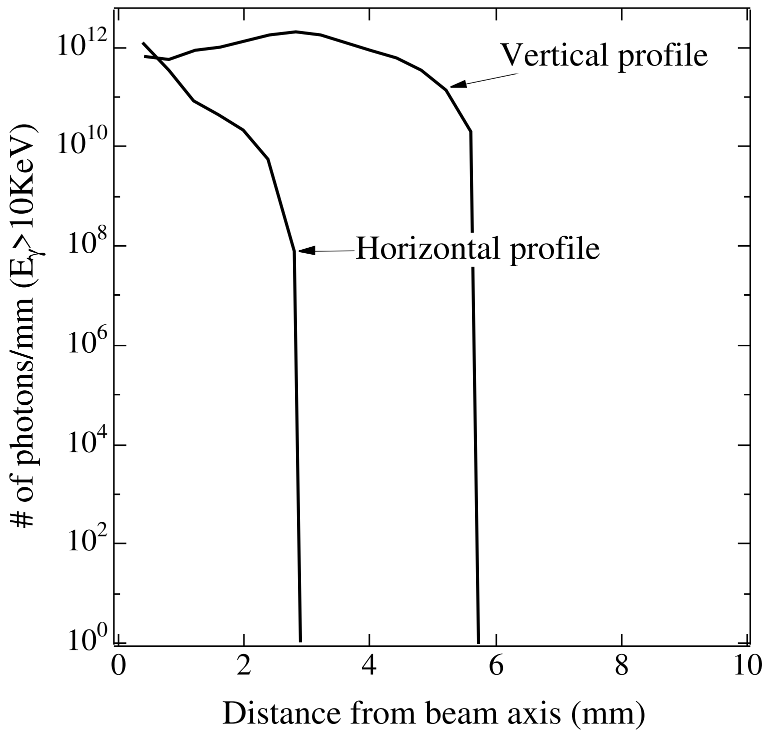

Figure 3.20: Profile of synchrotron radiation per train crossing from QC4-QC1 at the front face of QC1 seen from IP,*i.e.* 2.5m upstream from IP for E_{beam} =250GeV.

in horizontal and vertical directions, which correspond to $22\sigma_x$ and $264\sigma_y$, respectively, there is no emittance growth due to a wake field by the mask. There is no secondary particles ($e^{\pm}$'s and $\mu^{\pm}$'s) created at the mask because no beam tail can hit it. With this mask the synchrotron radiation is well collimated to 1 cm at IP.

B. Quadrupole Magnets

There are only 4 quadrupole magnets, QC1 - QC4, in a straight section between the last bending magnet and IP. Among them QC2 is the largest radiation source. Here we do not consider any mask since a doublet of final quadrupole magnets (QC1 and QC2) is so near IP that there is no way to stop back-scattered synchrotron radiations from the mask. The control of synchrotron radiations from the quadrupole magnets is uniquely provided by the optics of the final focus system. The optics is carefully determined in order to have a large bore (1.34 cm ϕ) of QC1, which is enough for the synchrotron radiations to go through without scattering for the beam collimated at $\pm 6\sigma_x$, $\pm 35\sigma_y$. The tail of the synchrotron radiations is also produced by the tail of beam. Figure 3.20 shows the lateral spread of radiations from QC3,QC4,QC2 and QC1 itself in front face of QC1, *i.e.* 2.5 m upstream of IP. Tolerable number of photons is $O(10^7)$ for x,y > 0.67cm in this figure, which may hit the "iron" pole of QC1 and back-scatter into IP. As discussed in the previous section there must be tails up to 10^4 photons beyond sharp cuts of the lateral spreads in Fig.3.20. We show Fig.3.21 to see how the radiations go through QC1. In Fig.3.21 cross sectional views of radiations are shown at the entrance and the exit of QC1. The two off-axis profiles are those of the radiations with exit beam (after collision) since a crossing angle is 8 mrad at E_{beam} =250GeV and QC1 is 2.4 m long, whereas the profile at the center is that of focusing beam (before collision). Therefore there is no serious background problem of the synchrotron radiations.

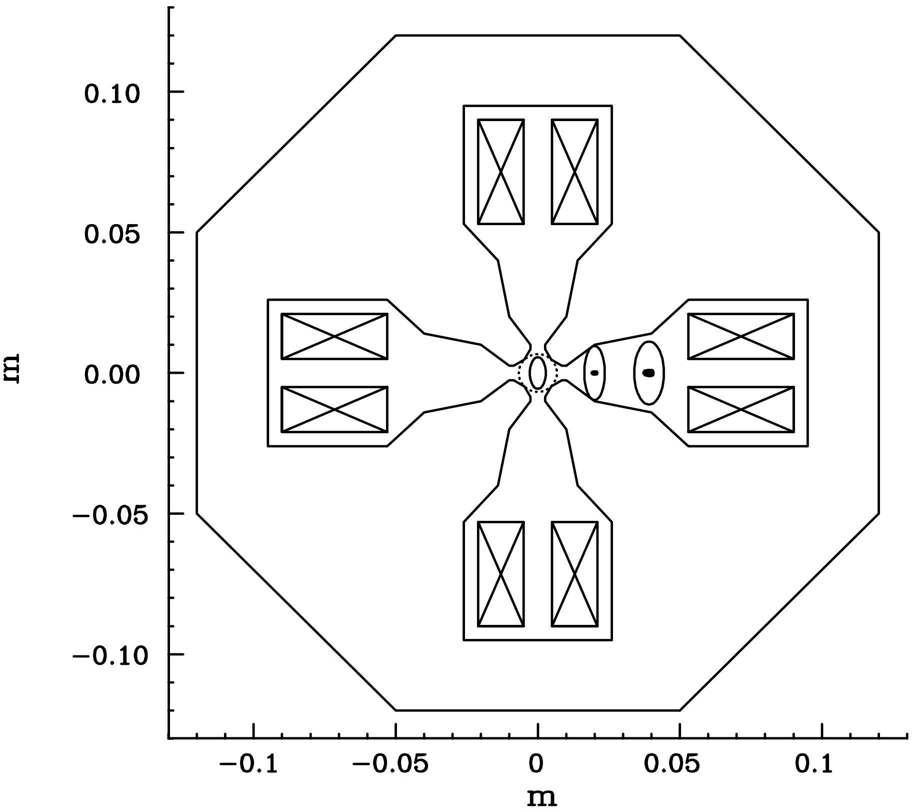

Figure 3.21: Cross sectional views of incoming and outgoing synchrotron radiations, which are shown as ellipses, at the entrance and exit of QC1, for E_{beam}=250GeV, where the crossing angle of two beams is 8 mrad. QC1 is located at 2.5m upstream from IP, and its half aperture and length are 6.7mm and 2.4m, respectively. Its coils are indicated by crosses boxes. Disrupted beams after collision are also plotted by dots.

3.7.4 e^+e^- pairs

e^+e^- pairs are created in coherent[16] and incoherent processes at linear colliders. The coherent process is the beamstrahlung photon conversion by a strongly collective magnetic field produced by the opposing beam. Its probability depends mainly on a beamstrahlung parameter(Υ). Since the condition of $\Upsilon \sim 1$ corresponds to a threshold for a photon of beam energy to convert into an e^+e^- pair in the magnetic field and the pair creation with $\Upsilon < 1$ is exponentially suppressed as $\exp(-16/8\Upsilon)$, coherent pairs is only relevant at a linear collider with $\Upsilon \geq 1$. For JLC- I the number of coherent pairs are negligibly small because of $\Upsilon = 0.093(0.19)$ at E_{beam}=150(250) GeV. On the contrary, the incoherent process comprising (a) BW (Breit-Wheeler): $\gamma\gamma \to e^+e^-$, (b)BH (Bethe-Heitler): $\gamma e^\pm \to e^\pm e^+e^-$, and (c)LL (Landau- Lifshits): $e^+e^- \to e^+e^-e^+e^-$ has no such energy threshold and it is proportional to luminosity, where γ is a beamstrahlung photon, and its number is about one per a beam particle for JLC-I. Their typical cross sections are (a)BW: $1.9 \cdot 10^{-27}\mathrm{cm}^2$, (b)BH: $2.2 \cdot 10^{-25}\mathrm{cm}^2$ and (c)LL: $4.5 \cdot 10^{-26}\mathrm{cm}^2$ at E_{beam}=250 GeV. As luminosity per bunch crossing is very high, which is $1.0 \cdot 10^{30}\mathrm{cm}^{-2}\mathrm{bunch}^{-1}$ at E_{beam}=250 GeV, enormous number of pairs are created at each collision, then they may kill an experiment.

The backgrounds of the pairs can be classified in two ways, *i.e.* (i) primary and (ii) secondary background. The former comprises pairs which directly enter a detector region, then overlap a physics signal. The most affective region of a detector is for a vertex detector because of the small transverse momenta of the pairs. The latter comprises secondary particles,*i.e.* neutrons and photons, which are created in a collision between the pairs and a pole tip of QC1. The number of neutrons(N_n) is proportional to the total deposit energy of the pairs (ΣE_e), *i.e.* $N_n \sim 0.13 \cdot \Sigma E_e$, while the number of photons(N_γ) is proportional to the total number of the pairs (ΣN_e), *i.e.* $N_\gamma \sim \Sigma N_e$. To quantitatively estimate these backgrounds we simulate the pairs by ABEL. For the generation of the pairs ABEL takes account of inherent scattering angles of the pairs, which can be larger than their characteristic angles of m_e/E_e, a geometric reduction due to smaller beam spot size (especially in vertical direction) than the typical impact parameters and an effect of strong external field. In ABEL the pairs are kicked by the strong electromagnetic field produced by the opposing beam, then they can acquire larger transverse momenta than the inherent ones. The final scattering angle (θ_e) is the sum of the inherent angle (θ_e°) and kick angle (θ_{kick}). The detailed description of this simulation is found elsewhere[17].

Figure 3.22 shows a scatter plot of the pairs in a plane of the final scattering angle (horizontal axis) and the transverse momentum (vertical axis). A sharp boundary is clearly seen in this figure, which corresponds to the maximum kick angle of the pairs ($\theta_e^\circ << \theta_{kick}$), and the pairs are seen to be also largely scattered beyond this boundary ($\theta_e^\circ >> \theta_{kick}$). The pairs in very forward angular region ($\theta_e < 0.15$) hit QC1 *etc.* , then the secondary photons are back-scattered. For further study of the primary background we plot the pairs of $\theta_e > 0.15$ (outside of a mask which is described in next section) as a function of their transverse momenta in Fig.3.23. The results are listed in Tab.3.5 for all cases of JLC-I at E_{beam}=150 and 250 GeV together with machine parameters relevant to background study. From ΣE_e's in Tab.3.5 the total number of neutrons is $O(10^6)$ per train crossing. Typical energy deposit of a neutron is estimated to be about 0.1 MeV, which is normalized to electron energy, with a detection efficiency of $< 50\%$ in our calorimeters[18]. Assuming the neutrons spread uniformly over 20k channel calorimeter, energy deposit per channel is a few MeV, *i.e.* $10^6 \cdot 0.1(\mathrm{MeV}) \cdot 0.5(\mathrm{eff.})/(2 \cdot 10^4)$. The other detector is less sensitive to neutrons. Therefore the neutrons cause no serious problem. Possible problems of secondary photons and backgrounds in a vertex detector will be discussed in subsequent sections.

Table 3.5: Characteristics of JLC-I

E_{beam} (GeV) Band	150 S	150 C	150 X	250 S	250 C	250 X
L (cm^{-2}sec^{-1}) $\times 10^{33}$	3.5	6.6	3.2	4.8	11.	6.3
L (cm^{-2}bunch^{-1}) $\times 10^{29}$	15.3	6.1	2.4	17.5	10.	4.7
rep. rate (Hz)	50	150	150	50	150	150
number of bunches	46	72	90	55	72	90
bunch separation	5.6ns	2.8ns	1.4ns	5.6ns	2.8ns	1.4ns
$N_{e^\pm}$/bunch $\times 10^{10}$	1.56	1.0	0.63	1.30	1.0	0.63
σ_x (nm)	335.	335.	335.	301.	260.	260.
σ_y (nm)	3.92	3.92	3.92	3.04	3.04	3.04
σ_z (μm)	80.	80.	85.	80.	80.	67.
β_x (mm)	10.	10.	10.	10.	10.	10.
β_y (μm)	100.	100.	100.	100.	100.	100.
D_x	0.21	0.13	0.090	0.13	0.13	0.071
D_y	18.0	11.5	7.7	13.0	11.5	6.1
disruption angle: $\theta_\circ$ (mrad)	0.88	0.57	0.35	0.49	0.44	0.27
crossing angle: ϕ_c (mrad)	11.0	10.4	9.0	7.3	8.0	7.2
$\langle\Upsilon\rangle$	0.14	0.093	0.059	0.23	0.19	0.15
Υ_{max}	0.47	0.32	0.19	0.78	0.70	0.51
energy loss (δ) (%)	7.0	3.5	1.7	9.0	7.0	4.0
n_γ	1.7	1.1	0.74	1.6	1.4	0.91
A	1.3	0.95	0.74	1.0	0.93	0.66
$1.65 \times P_t^{max}$ (MeV)						
at θ =0.15	26.9	17.2	10.3	22.9	18.2	13.2
R_{mask} (cm)	9.0	5.7	3.5	7.7	6.1	4.4
L_{mask} (m)	0.60	0.38	0.23	0.51	0.41	0.29
$\eta_{mask}(L_Q = 2.5\text{m}) \times 10^{-4}$	6.0	1.9	0.60	3.9	2.2	1.0
total energy deposits(GeV)						
and e's/bunch						
ΣE_e(no θ_e cut) $\times 10^5$	1.8	0.60	0.17	5.8	3.0	0.91
ΣN_e(〃) $\times 10^4$	6.2	2.0	0.62	7.0	3.9	1.3
$\Sigma E_e(\theta_e > .005) \times 10^4$	13.	4.0	0.55	11.	5.8	1.3
ΣN_e(〃) $\times 10^4$	5.4	1.7	0.49	5.1	2.8	0.96
$\Sigma E_e(\theta_e > .050) \times 10^2$	5.4	4.9	0.94	21.	9.2	2.2
ΣN_e(〃) $\times 10^3$	8.0	5.7	1.0	11.	9.4	3.2
number of hits(e's)/bunch						
in $\lvert\cos\theta_e\rvert < 0.9$						
$r = 2$ cm	429.4	117.8	63.1	350.2	100.4	81.6
	(188.5)	(21.1)	(5.8)	(69.8)	(34.4)	(11.1)
$r = 5$ cm	76.8	7.3	124.	51.7	21.7	23.3
	(14.6)	(4.7)	(2.8)	(10.9)	(6.8)	(2.9)
$r = 30$ cm	2.3	1.1	0.	1.4	0.3	0.3
	(1.0)	(0.5)	(0)	(0.75)	(0.2)	(0.2)

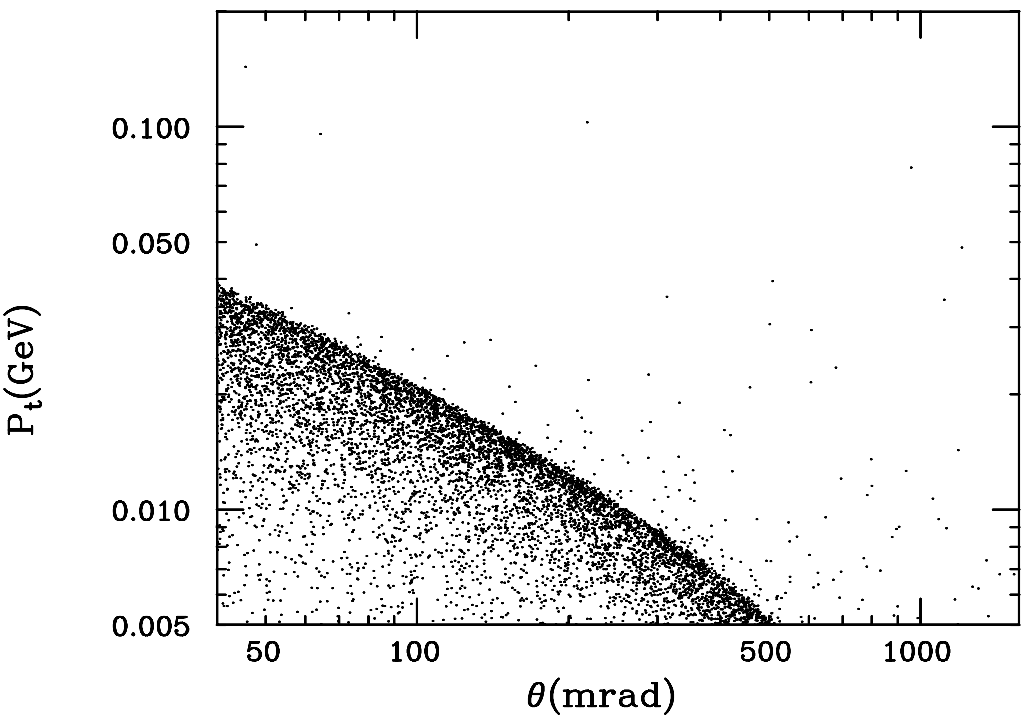

Figure 3.22: Pairs simulated by ABEL on a plane of p_t and θ_e at E_{beam}=250GeV for JLC-I(c-band).

3.7.5 Masking System

Our masking system is schematically shown in Fig.3.24. A mask is employed in order to shield against the large amount of the secondary photons. The probability for the O(10^7) photons/train (see Tab.3.5) to escape from the mask, η_{mask}, should be less than 10^{-3}, which is geometrically determined by the front aperture of the mask. Most of the escaped photons hit the mask surface on the opposite side, then they enter the detector region. In addition the mask must have enough thickness to absorb the photons, that is, its attenuation coefficient should be less than 10^{-5} for 0.5MeV photons which corresponds to a 5cm thick tungsten. We require that the acceptable number of photons in the detector region is O(10^2) per train crossing. As we fix the angular region of the mask as $0.15 < \theta_{mask} < 0.2$, it remains to determine only one parameter to fully specify the geometry of the mask. We take the half aperture of the mask, R_{mask} in Fig.3.24, for this parameter. R_{mask} can be linearly related to a diameter of circular trajectory of a charged track in a solenoidal magnetic field(B), *i.e.* $R_{mask} = p_t^{max}/0.15B$ and B=2Tesla. We determine R_{mask} for the pairs, which comprise a shoulder in Fig.3.23, to loop inside the mask. There is another important constraint from the solid angle seen by the photons back-scattered at QC1, *i.e.* $\eta_{mask} = R_{mask}^2/4(L_Q - L_{mask})^2 < 1 \times 10^{-3}$, where L_{mask} and L_Q are the distances of the mask and the final focus quadrupole magnet from the interaction point(IP), respectively(Fig.3.24). The location of the final focus quadrupole magnet has been set to be 2.5 m from IP for the synchrotron radiations to go through QC1 without scattering as mentioned in the previous section. The optimized values of R_{mask}, L_{mask} and η_{mask} are also listed in Tab.3.5. With this masking system, the total number of charged particles hitting the outer surface of the mask is less than 10^3/train(72 bunches) as shown in Fig.3.23.

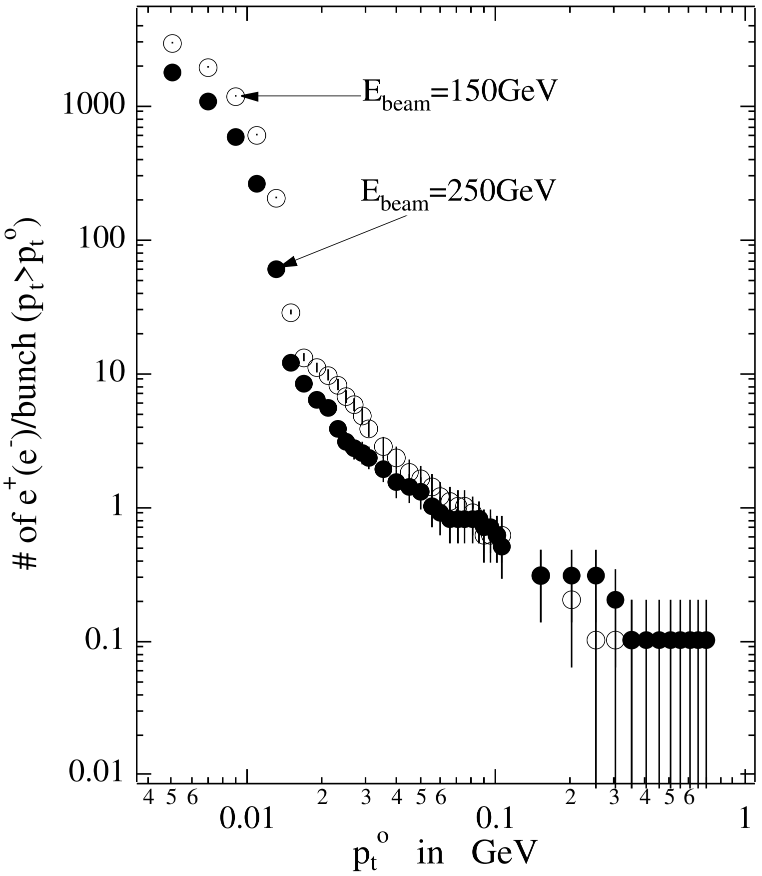

Figure 3.23: Pair yield/bunch crossing as a function of P_t° for $\theta_e > 0.15$ at JLC-I(c-band).

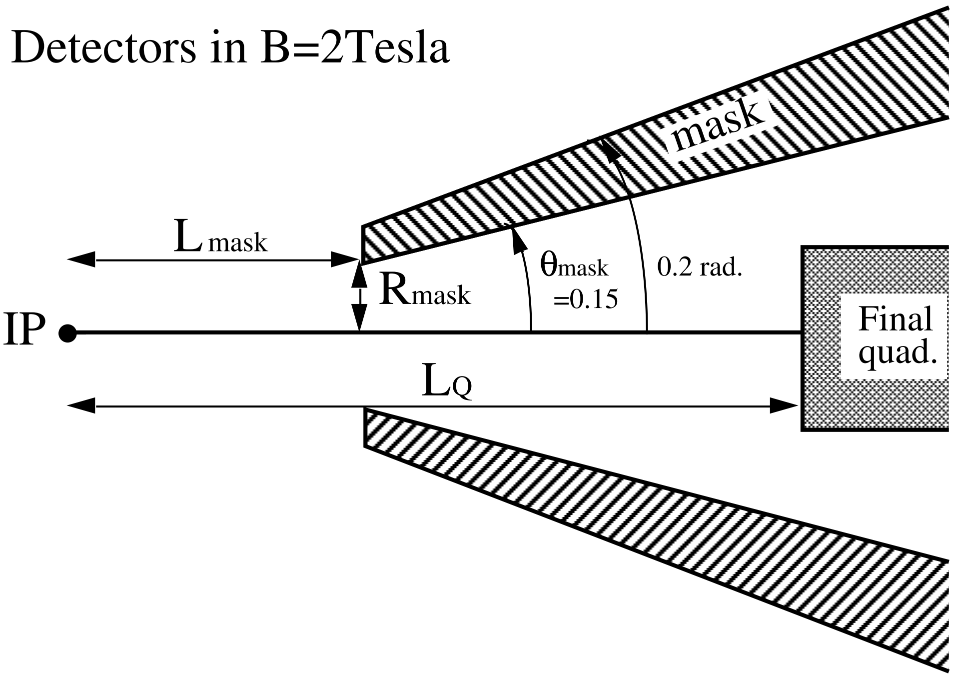

Figure 3.24: A masking system at the interaction region

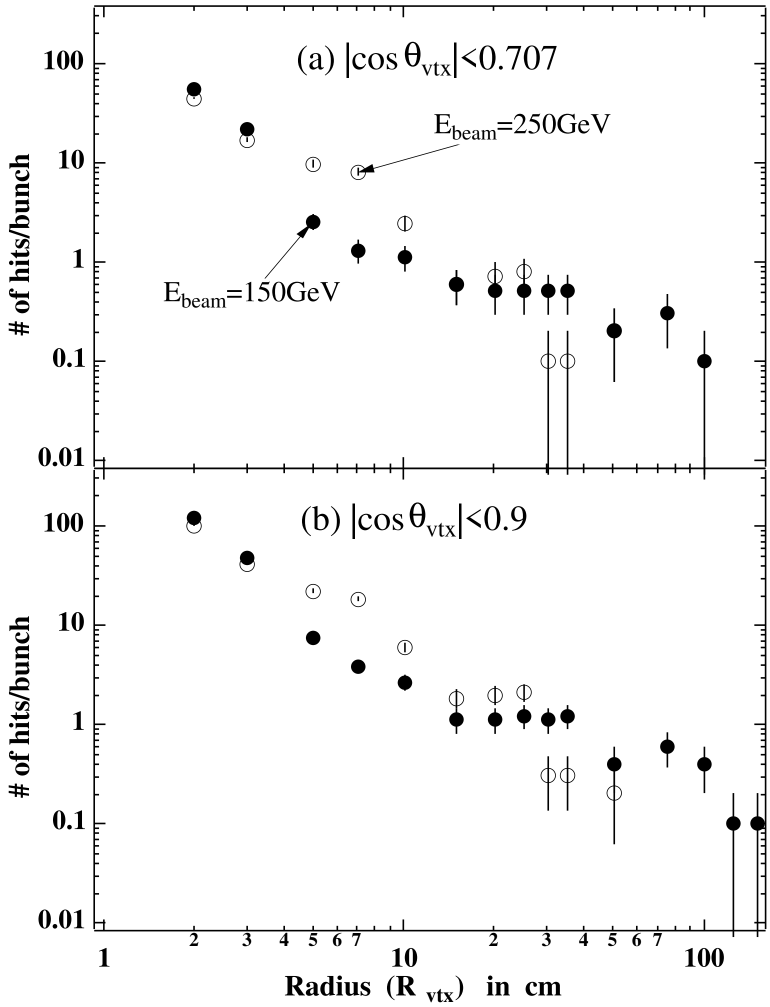

Figure 3.25: background hits by the pairs in B=2Tesla as a function of radius(R_{vtx}.

3.7.6 Background at the Vertex Detector

In general we can use a beampipe of small radius, e.g. $R_{pipe} \sim$ 1cm, at IP because of no fear of synchrotron radiation as discussed in the previous section. Therefore, a vertex detector can be placed very close to the beam line. In order to estimate the background in the vertex detector, the number of hit points , which the pairs make by traversing the surface of the cylinder of radius R_{vtx} and length $Z_{vtx} = R_{vtx}/\tan\theta_{vtx}$ around the collision point, are plotted as a function of R_{vtx} at $|\cos\theta_{vtx}|$=0.707 and 0.9 in Fig.3.25(a),(b). Here we assume the helix trajectories of the pairs in the solenoidal magnetic field of 2 Tesla and we allow for the pairs to register multiple hit points without any interaction. The number of hits decreases rapidly as R_{vtx} increases. The hit numbers per bunch crossing are 117.8(21.1) and 100.4(34.4) at R_{vtx}=2cm, $|\cos\theta_{vtx}|$=0.9 for JLC-I(c-band) E_{beam}=150 and 250GeV, respectively, where values in parenthesis are the number of particles which make hits. The hit numbers have to be multiplied by 72 for a real background estimation because there are 72 bunches/train. This background apparently prevents us from using a gas chamber as the vertex detector in R_{vtx} <10cm. Our CCD(pixel) device is the best detector. The vertex detector also suffers from the secondary photons. Since the number of these photons is on the order of 10^3 per train crossing, the corresponding hit number in the vertex detector is always less than those of the pairs with a few % of the conversion probability of the photons.

3.8 The Underlying Hadronic Background

The two-photon hadronic background is one of the most important issues in the future e^+e^- linear collider experiments, since which might spoil the clean experimental environment otherwise available. The higher the energy, the severer the problem becomes because of the following reasons.

1. Since the bremsstrahlung photon intensity increases with energy as $\ln(\sqrt{s}/m_e)$, the cross section of a two-photon process increases as, $\sigma \propto (\ln s/m_e)^2$. In addition, according to the DG model[24], the minijet production rate increases as $\sigma \propto (\sqrt{s})^{1.4}$. Therefore, for example, the cross section of the minijet production increases by about a factor of 20, when we go up from the TRISTAN energy region to that of JLC-I.

2. There are, in addition, beamstrahlung photons, whose contribution to the minijet events is comparable to or even larger than that of the bremsstrahlung photons.

3. At linear colliders, the beam size is significantly smaller than that of the present circular colliders and the luminosity per beam crossing is much larger. It is 0.1 mb^{-1} per beam bunch crossing at TRISTAN, while it is 66 mb^{-1} at JLC-I. Since there are about 100 bunches per RF pulse of width 100 to 300 nsec, the effective luminosity for the detector increases further, if it cannot distinguish signals from different bunches.

In the following, we estimate the rate of the hadronic background at JLC-I and show that the rate is low enough to achieve a clean experimental environment, if the detector has a good timing resolution as described in the previous sections.

3.8.1 The Model

We calculate the cross section for the two-photon hadron productions, using the DG model[19] and the VDM model. The cross sections are given by

$$\sigma = \int f_{e^-/\gamma} f_{e^+/\gamma} \bar{\sigma}\, dx_1 dx_2,$$

where the two-photon cross section $\bar{\sigma}$ depends on models:

$$\bar{\sigma} = A + B/W_{\gamma\gamma},$$

with $A = 240$ nb and $B = 270$ nb·GeV for the VDM model, and

$$\bar{\sigma} = \int_{P_{T,min}} D_{\gamma/p}(Q^2, x_3) D_{\gamma/p}(Q^2, x_4) \frac{d\hat{\sigma}}{d\cos\hat{\theta}} dx_3 dx_4 d\cos\hat{\theta},$$

for the DG model. $f_{e^\pm/\gamma}$ is a γ density function inside $e^\pm$, $D_{\gamma/p}$ is a parton (photon, gluon, or quark) density function inside γ, and $\frac{d\hat{\sigma}}{d\cos\hat{\theta}}$ represents the differential cross sections of subprocesses. $\hat{\theta}$ is the scattering angle of the subprocess in the CM system. x_1 and x_2 are photon energies scaled by beam energy, and x_3 and x_4 are parton energies scaled by the original photon energy. As the energy scale, we took $Q^2 = \hat{s}/4$, where $\hat{s} = x_1 x_2 x_3 x_4 s$ and $s = 4E_{beam}^2$.

As $f_{e^\pm/\gamma}$, we use the Equivalent Photon Approximation function for the bremsstrahlung photons and the analytical formula derived by K. Yokoya and P. Chen[26] for the beamstrahlung photons. The details can be found in [25].

It was reported that, in the TRISTAN energy region, the sum of the DG model and the VDM model well describes the two-photon hadron production data without electron-tag, when $p_{T,min}$ of the DG model is 1.6 GeV[20, 21]. The extrapolation of the models to higher energies, however, suffers from some ambiguities. The parton density functions inside the photon, especially the low x behaviors, still need experimental determinations. J. R. Forshaw and J. K. Storrow pointed out that the eikonalization would reduce the minijet cross section by about a factor of 5 at $\sqrt{s} = 500$ GeV[23], though its proper treatment is not clear. Since our calculation does not include the eikonalization,the background estimate presented below is conservative.

3.8.2 The Background Yield

The calculated background rates are summarized in Table 3.6. The total minijet cross sections at $\sqrt{s} = 300$ and 500 GeV obtained from the DG model are shown in Fig. 3.26, as a function of $p_{T,min}$, for the bremsstrahlung photons and the beamstrahlung photons corresponding to the three machine parameters shown in Table 4.1.

As seen in the figure and the table, the main source of the background is the beamstrahlung photons, except for the X-band JLC at $\sqrt{s} = 300$ GeV. The background rate at the lower frequency machine is larger than that of the higher frequency machine because the number of beamstrahlung photons is larger in the lower frequency machine due to larger number of particles/bunch. In the table, the number of minijet events is estimated using $P_{T,min}$ =1.6 GeV. If we use $P_{T,min} = 2$ GeV as suggested by the preliminary TOPAZ results[22], the number of minijet events will be reduced by about a factor of 3. In any case, the rate expected from the VDM model is larger than that of the DG model at JLC-I. The actual rate is the sum of the DG model and the VDM model. The number of background events per RF pulse is greater than one, which is reduced when the detector can separate signals from different bunches as described in the previous sections. In this case, the probability to have a background event in a signal event is about 2% to 25%, depending on the beam energy and the machine parameters.

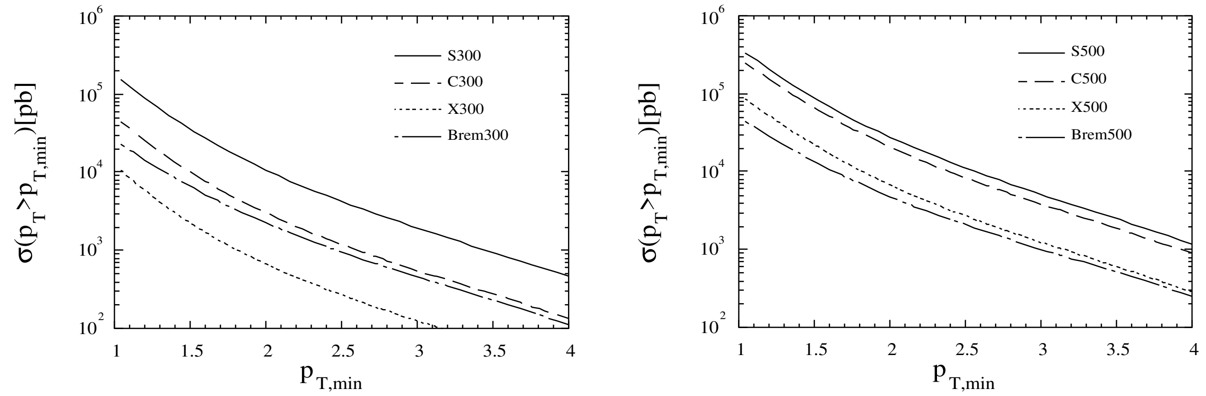

(a) (b)

Figure 3.26: The total minijet cross section integrated from $p_{T,min}$ to the maximum at (a) $\sqrt{s} = 300$ and (b) $\sqrt{s} = 500$ GeV, as a function of $p_{T,min}$, using the DG parameterization. The solid, dashed, and dotted curves show the cross sections due to the beamstrahlung photons of S-, C-, and X-band designs, respectively. The dot-dashed curves show those due to the bremsstrahlung photons.

E_{beam} (GeV)	$\sqrt{s} = 300$ GeV			$\sqrt{s} = 500$ GeV		
RF frequency	S band	C band	X band	S band	C band	X band
# particles/bunch ($\times 10^{10}$)	1.73	1.11	0.70	1.45	1.10	0.70
Bunch spacing (nsec)	5.6	2.8	1.4	5.6	2.8	1.4
Repetition rate (Hz)	50	150	150	50	150	150
# bunches/pulse	46	72	90	55	72	90
# of beamstrahlung photons	1.80	1.19	0.80	1.62	1.44	0.95
Luminosity/pulse (μb^{-1}/pulse)	62	39	23	88	64	42
by the DG model						
$\sigma(p_T > 1.6$ GeV) (μb)	0.032	0.013	0.007	0.079	0.062	0.028
σ_{beam}	0.027	0.0076	0.0017	0.068	0.051	0.017
# events/pulse	2.0	0.51	0.16	7.0	4.0	1.2
# events/bunch	0.043	0.0071	0.0018	0.13	0.056	0.013
P_{clean}	0.958	0.993	0.998	0.88	0.946	0.987
by the VDM model						
$\sigma(W_{\gamma\gamma} > 2$ GeV) (μb)	0.15	0.081	0.051	0.18	0.16	0.11
σ_{beam}	0.11	0.048	0.018	0.10	0.082	0.034
# events/pulse	9.1	3.2	1.2	15	10	4.6
# events/bunch	0.20	0.022	0.013	0.28	0.14	0.05
P_{clean}	0.819	0.978	0.987	0.756	0.869	0.951

Table 3.6: The summary of the background event rates. σ_{beam} is the background cross section due to the collision between beamstrahlung photons. P_{clean} is a probability to have an event without background: $P_{clean} \equiv e^{-<n>}$ where $< n >$ is the average number of background events.

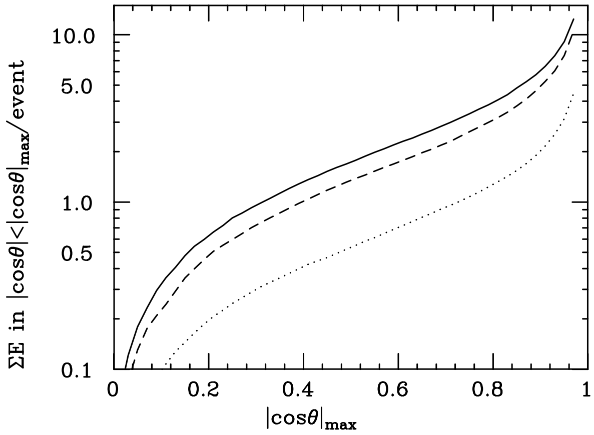

Figure 3.27: The energy deposit of a minijet event in the central region as a function of the maximum $|\cos\theta|$. The solid curve and the dashed curve are the simulation results for the DG model using the independent fragmentation and the string fragmentation, respectively. The dotted curve is for the VDM model. The beam energy is 150 GeV.

3.8.3 Effect on Physics Analyses

The energy deposit of a minijet event to the detector is estimated by Monte Calro simulations. In the simulation with the DG model, the spectator partons in the resolved process are produced along the beam axis, and subsequently hadronized together with the hard-scattered partons by the independent fragmentation or the string fragmentation. In the case of the VDM model, two quarks are generated with the angular distribution of $d\sigma/dp_T = e^{-4p_T^2}$ and hadronized by the string fragmentation. According to the simulations, a DG-model event produces about five charged tracks on the avergae in the region $|\cos\theta| < 0.866$. The sum of the energy deposit to the central region of the detector is shown in Fig. 3.27, as a function of the maximum $\cos\theta$. From the figure, we conclude that the energy deposit, for example, in the region of $|\cos\theta| < 0.9$ is 6 , 5, and 2 GeV for the DG with the independent fragmentation, the DG with the string fragmentation, and the VDM model, respectively. If we sum up these numbers weighted by the probability to have background events, the average energy deposit to the detector region of $|\cos\theta| < 0.9$ is less than about 0.6 GeV at $\sqrt{s} = 300$ GeV, which is about 0.2 % of the center of mass energy. Therefore, the effect of the background should be negligible.

As an example of the effect of the minijet background on physics analyses, we show, in Fig. 3.28, the invariant mass distribution of the two jets for the process $e^+e^- \to Z^0H^0$, when one minijet event of the DG-type overlaps every signal event. Although the measured width of the Higgs signal increases from 3.9 GeV to 5.3 GeV, we can still see a clear Higgs signal over the background from the $e^+e^- \to ZZ$ process. Note that the minijet background yield assumed in Fig. 3.28 is at least 20 times larger than our pessimistic estimate.

In conclusion, the hadronic background at JLC-I will not spoil the cleanness of the e^+e^- collisions, if the detector can separate signals from different bunches. Even if the background rate is 20 times larger than that expected from the DG model, we can observe a clear Higgs signal, if the Higgs is in the region accessible by JLC-I.

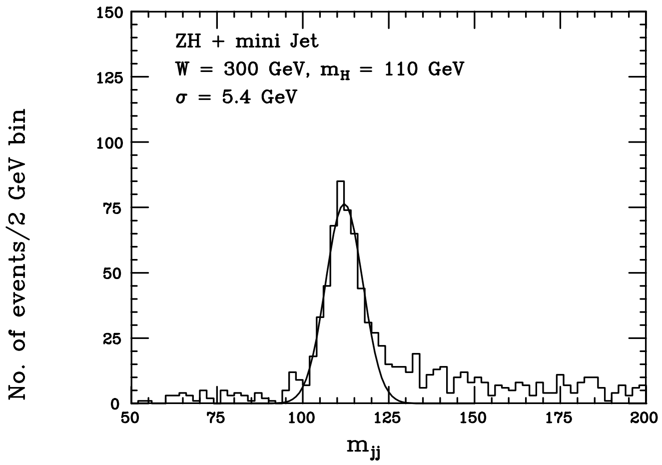

Figure 3.28: The invariant mass of the two-jet system for the process $e^+e^- \rightarrow Z^0H^0$ in a 4-jet mode, when one minijet event overlaps every signal event, at $\sqrt{s} = 300$ GeV and when $M_H = 110$ GeV. The integrated luminosity is 25 pb^{-1} and other conditions are the same as those used in Fig. 3.11.

3.9 Data Acquisition and Trigger

3.9.1 Channel Count and Read-out Scheme

The total number of channels and a typical data size of each detector part are summarized in this section. A brief summary of the trigger scheme is also given.

Vertex Detector

The vertex detector consists of 6k pads of CCD's which have 64k pixel's each. The number of channels is 4×10^8 channels in total. To separate a minimum-ionizing particle signal from thermal noise, a five σ cut from the thermal noize peak is enough. The number of hits caused by thermal noize is estimated to be 12k hits. The number of hits of the background tracks generated by beamstrahlung photons and so on is estimated to be 5 k hits based on the Tauchi's background study. The number of hits of signal tracks is negligible. The typical number of hits per beam crossing is 17k channels which corresponds to 68 kbyte of data size. The induced signals in the pixel's are fed to Flash ADC's serially and stored in the data memories.

Central Drift Chamber

The total number of read-out wires of the CDC is 1.7×10^4 wires (both sides of 8.4×10^3 sense wires). The signal shape is recorded by 200 MHz flash ADC's in 5 μsec. The total number of channels is 1.7×10^7. The number of hits by soft-photons coming from the beam mask in front of the final Q-magnet is estimated to be 8×10^2 hits per beam crossing. The number of hits from mini-jet background is 2×10^4 for the worst case. The number of tracks from, for example, W-pair production, which decay hadronically, is about forty. Thus the number of hits per event is 8×10^3. If we smple the data during 500 μsec around the signal, one hit has 100 bins each. The typical event size of one hadronic event is 12 Mbyte.

Calorimeter

The calorimeter consists of 5×10^3 towers of a electromagnetic ($ECAL$) and hadronic ($HCAL$) calorimeter. Since each tower has one $HCAL$ module, four $ECAL$ modules, and 400 Si pads, the calorimeter has 2×10^6 channels in total. The parallel data from 400 Si pads are multiplexed and are serially fed to a ADC. The typical channel counts for a hadronic event is 7.5×10^3, which corresponds to 30 kbyte.

Muon Detector

The muon detector consists of six super-layers of single-cell drift chambers and one layer of plastic scintillation counters. The total number of channels is 7700 channels for the barrel part and 2400 channels for each endcap part. In total the data size of the muon detector is 40kbyte. The typical data size for one beam-crossing depends on the muon background from the final focus part. Muons will be swept away by toroidal magnets set along a beam line. At any rate, the data size from the muon detector is negligible compared with other detector parts.

3.9.2 Trigger Philosophy

We do not have any first-level triggers. In each beam crossing, all data will be stored in memories. A trigger decision will be done based on fast-tracking information and calorimeter information before the next beam crossing which comes 5 msec later. The CDC and CAL are divided into several segments azimuthally including overlap regions. High speed workstations will perform fast-tracking and energy clustering within each segment. A master computer will combine tracking and clustering information from each detector-segment and make a decision to store the data into mass storage or not. The trigger criteria may be easily defined by editing a table. The events which only have the mini-jets are rejected at this stage. The trigger rate is expected to be several Hz, thus, there are no problems with data transfer and mass storage.

Subsystem	Channel Count		typical data size (byte)
	total	one event	
Vertex detector			
thermal noise		12k	48k
BG track		5k	20k
signal track		-	-
Subtotal	400M	17k	68k
Central tracker			
soft photon		80k	0.32M
mini jet		2M	8.0M
jet track		800k	3.2M
Subtotal	17M	2.9M	12M
Calorimeter			
EM	20k	1.2k	4.8k
HD	5k	0.3k	1.2k
Si	2M	6k	24k
Subtotal	2M	7.5k	30k
Muon detector			
barrel	7.7k	-	-
endcap	2.4k	-	-
Subtotal	10k	-	-
Total	405M	3M	12M byte

Table 3.7: Channel count requirement.

Bibliography

[1] T. Tauchi, et al., *KEK Preprint* 90-181 (1991).
P. Chen and V. I. Telnov, *SLAC-PUB*-4923 (1989).
T. Tauchi, K. Yokoya, and P. Chen, *SLAC-PUB*-5557 (1991).

[2] M. Drees and R. M. Godbole, *Phys. Rev. Lett.* **67** (1991) 1189.

[3] A. Miyamoto, *Proceedings of the Third Workshop on Japan Linear Collider*, KEK, 1992, ed. by A. Miyamoto, *KEK Proceedings 92-13*, December, 1992.

[4] C. Adolphsen and D. Burke, private communication.

[5] Y.Fujii, *Proceedings of the Third Workshop on Japan Linear Collider*, KEK, 1992, ed. by A. Miyamoto, *KEK Proceedings 92-13*, December, 1992.

[6] E.Bernardi *et.al.*, *Nucl. Instr. Meth.* **A262** (1987) 229.

[7] D.Acosta *et.al.*, *Nucl. Instr. Meth.* **A308** (1991) 481.

[8] C.Zeitnitz *et.al.*, *DESY 92-045*, March, 1992.

[9] H. Fenker, *SSCL-Preprint-120*, May, 1992.

[10] W.R. Nelson and Y. Namito, MUON89 code for calculation of muon shielding.

[11] E.A. Kushnirenko, "MUON ATTENUATION", presented at FFIR workshop at SLAC, March,1992.

[12] Y. Namito, a detailed simulation is under going.

[13] J.Irwin, "Collimating MegaWatt Micron Sized 250-500 GeV Electron Beams", presented at LC92 at Garmisch-Partenkirchen Germany, July,1992.

[14] K.Yokoya, private communication, and also presented at LC91 at Protvino Russia, September,1991.

[15] W. Lohmann, R. Kopp and R. Voss, *CERN 85-03*, March, 1985.

[16] P. Chen and V.I. Telnov, *Phys. Rev. Lett.* **63** (1989) 1796.

[17] T. Tauchi, K. Yokoya and P. Chen, to be published in *Particle Accelerators* .

[18] T.Tauchi *et al.*, "Background Problem at Interaction Point for an e^+e^- TeV Linear Collider" Presented at the DPF Summer Study on High Energy Physics: Research Directions for the Decade, Snowmass, Colorado, June 25-July 13, 1990, SLAC- PUB-5652.

[19] M. Drees and R. M. Godbole, *Nucl. Phys.* **B339** (1990) 355; *Phys. Rev. Lett.* **67** (1991) 1189.

[20] R. Tanaka, *et al.*, *Phys. Lett.* **B277** (1992) 215.

[21] H. Hayashii, NWU-HEP 92-03, June 1992. To appear in the proceeding of the 9th International Workshop on Photon-Photon collisions, San Diego, USA, March, 1992.

[22] M. Iwasaki, talk presented at the JPS meeting, Niigata, September, 1992.

[23] J. R. Forshaw and J. K. Storrow, *Phys. Lett.* **B268** (1991) 116; *Phys. Lett.* **B278** (1992) 193.

[24] M. Drees and R. M. Godbole, *DESY 92-044*, March, 1992.

[25] A. Miyamoto, *Proceedings of the Third Workshop on Japan Linear Collider*, KEK, 1992, ed. by A. Miyamoto, *KEK Proceedings 92-13*, December, 1992.

[26] K. Yokoya, private communication. see also P. Chen, *SLAC-PUB-5615.*